Journal of Theoretical Biology 545 (2022) 111104

Contents lists available at ScienceDirect

Journal of Theoretical Biology

journal homepage: www.elsevier.com/locate/yjtbi

A DNA-structured mathematical model of cell-cycle progression in cyclic hypoxia

Giulia L. Celora [a,*], Samuel B. Bader [c], Ester M. Hammond [c], Philip K. Maini [a], Joe M. Pitt-Francis [b], Helen M. Byrne [a]

[a] Mathematical Institute, University of Oxford, Oxford, UK
[b] Department of Computer Science, University of Oxford, Oxford, UK
[c] Oxford Institute for Radiation Oncology, Department of Oncology, University of Oxford, Oxford, UK

ARTICLE INFO

Article history:
Received 17 August 2021
Revised 15 March 2022
Accepted 18 March 2022
Available online 23 March 2022

Keywords:
Cell-cycle
Cyclic hypoxia
Cancer
Delay-differential equation
Model calibration
Model selection

ABSTRACT

New experimental data have shown how the periodic exposure of cells to low oxygen levels (*i.e.*, cyclic hypoxia) impacts their progress through the cell-cycle. Cyclic hypoxia has been detected in tumours and linked to poor prognosis and treatment failure. While fluctuating oxygen environments can be reproduced *in vitro*, the range of oxygen cycles that can be tested is limited. By contrast, mathematical models can be used to predict the response to a wide range of cyclic dynamics. Accordingly, in this paper we develop a mechanistic model of the cell-cycle that can be combined with *in vitro* experiments to better understand the link between cyclic hypoxia and cell-cycle dysregulation. A distinguishing feature of our model is the inclusion of impaired DNA synthesis and cell-cycle arrest due to periodic exposure to severely low oxygen levels. Our model decomposes the cell population into five compartments and a time-dependent delay accounts for the variability in the duration of the S phase which increases in severe hypoxia due to reduced rates of DNA synthesis. We calibrate our model against experimental data and show that it recapitulates the observed cell-cycle dynamics. We use the calibrated model to investigate the response of cells to oxygen cycles not yet tested experimentally. When the re-oxygenation phase is sufficiently long, our model predicts that cyclic hypoxia simply slows cell proliferation since cells spend more time in the S phase. On the contrary, cycles with short periods of re-oxygenation are predicted to lead to inhibition of proliferation, with cells arresting from the cell-cycle in the G2 phase. While model predictions on short time scales (about a day) are fairly accurate (*i.e*, confidence intervals are small), the predictions become more uncertain over longer periods. Hence, we use our model to inform experimental design that can lead to improved model parameter estimates and validate model predictions.

1. Introduction

The cell-cycle is one of the most fundamental and energy consuming processes in cell biology. It is divided into four phases: G1 (growth), S (DNA synthesis), G2 (growth and preparation for mitosis) and M (mitosis). Transitions between these phases are regulated by complex interactions between cellular pathways and external stimuli which normally act to maintain tissue homeostasis. These interactions are impaired in transformed cells, leading to uncontrolled proliferation, which is a key hallmark of cancer (Hanahan and Weinberg, 2000). Cell-cycle dysregulation is further linked to the hallmarks of cancer because it promotes genetic instability, *i.e.*, increasing mutation frequency (Negrini et al., 2010). In normal cells, the DNA damage response (DDR) maintains genetic stability by promoting cell-cycle arrest to allow time for DNA repair or, when DNA damage is irreparable, by promoting cell death via the induction of apoptosis. The DDR is activated early during tumourigenesis as an anti-cancer barrier to oncogene activity and physiological stresses (Bartkova et al., 2005; Gorgoulis et al., 2005). However, continuous activation of the DDR results in selective pressure for the outgrowth of mutated cancer cells, with aberrant cell-cycle progression and apoptotic control (Begg and Tavassoli, 2020; Gorgoulis et al., 2005). Loss of cell-cycle control also plays a significant role in the failure of standard treatments, such as chemotherapy and radiotherapy, where treatment relapse is driven by the emergence of small subpopulations of resistant cells. Exposure to insufficient oxygen levels, i.e., *hypoxia*, is a key driver of tumorigenesis. Hypoxic regions are commonly found in solid tumours (Barker et al., 2015; Good and Harrington, 2013; Kirkpatrick et al., 2004; Koumenis and Wouters, 2006) as a result of uncontrolled cell proliferation and abnormal vascular

* Corresponding author.
E-mail address: celora@maths.ox.ac.uk (G.L. Celora).

https://doi.org/10.1016/j.jtbi.2022.111104
0022-5193/

structures. Exposure to severe levels of hypoxia ($< 0.1\%\ O_2$), which are only observed in pathophysiological conditions, leads to replication stress and consequent activation of DDR and the pro-apoptotic p53 tumour suppressor (Foskolou et al., 2017; Leszczynska et al., 2016; Olcina et al., 2013). Further, conditions of less than $0.1\%\ O_2$ are associated with resistance to radiotherapy and are therefore commonly referred to as radio-biological hypoxia (RH) (West and Slevin, 2019).

Our study is motivated by evidence that the tumour microenvironment is characterised by highly dynamic oxygen levels. While chronic hypoxia affects tumour regions at a significant distance from vessels, acute/cycling hypoxia can occur close to, and far from, blood vessels, with periods ranging from seconds to hours/days (Ron et al., 2019). While high frequency fluctuations are usually associated with vasomotor activity, processes that occur on longer time scales (*e.g.*, vascular remodelling) can generate cycles with longer periods (Michiels et al., 2016). Such periodic changes in the environment are known to cause inflammation, which promotes the survival of more aggressive forms of cancer that are resistant to standard treatments (Bader et al., 2021; Begg and Tavassoli, 2020; Bristow and Hill, 2008; Michiels et al., 2016; Saxena and Jolly, 2019; Simms et al., 2012).

It is possible to culture cells *in vitro* in controlled oxygen environments that partially mimic the fluctuating oxygen levels experienced by tumours *in vivo*. However, *in vitro* experiments are limited by the range of oxygen cycles that can be tested. By contrast, mathematical models can provide insight into a wider range of experimental conditions. Our aim in this work is therefore to develop a novel mechanistic model of the cell-cycle that can be combined with *in vitro* experiments, to increase our understanding of how cyclic hypoxia impacts the cell-cycle.

When exposed to radio-biological hypoxia (RH) *in vitro*, progress through S phase is inhibited due to a rapid reduction in the rate of DNA synthesis (Foskolou et al., 2017; Pires et al., 2010). This hypoxia-induced S phase block has been attributed to impaired functioning of the enzyme ribonucleotide reductase (RNR) (Foskolou et al., 2017; Olcina et al., 2010), which mediates *de novo* production of *deoxynucleotide triphosphates* (dNTPs). Since dNTPs are the building blocks of DNA, the decrease in dNTP levels in severe hypoxia causes DNA synthesis to stall. In contrast, milder levels of hypoxia ($1 - 2\% O_2$) do not impact dNTP levels (Foskolou et al., 2017). Replication stress, which is defined as any condition impacting normal DNA replication, leads to activation of the DDR when local oxygen levels are sufficiently low. While cells can initially survive at such low oxygen levels, if severe conditions are prolonged then cell death occurs (Pires et al., 2010). Alternatively, if oxygen levels are restored, cells can re-enter the cell-cycle although they may accumulate DNA damage, likely associated with the accumulation of reactive-oxygen species (ROS) during reoxygenation (Michiels et al., 2016). Depending on the amount of damage sustained, activation of cell-cycle checkpoints causes cells to accumulate in the G2-phase and prevents damaged cells from entering mitosis (Bristow and Hill, 2008; Goto et al., 2015; Olcina et al., 2010). Alternatively, if the reoxygenated cells are unable to repair the damage accumulated, they die. Periodic exposure to RH (cyclic hypoxia) may therefore lead to cell death and strong selective pressure for more aggressive clones with impaired checkpoint activation.

Common techniques for monitoring cell-cycle dynamics include flow cytometry and time-lapse microscopy using the fluorescent ubiquitination-based cell-cycle indicator (FUCCI). Both methods can be used to indirectly estimate how the fraction of cells in different stages of the cell-cycle changes over time, by measuring either DNA content (flow cytometry) or expression of cell-cycle related proteins (FUCCI). Since we have access to flow cytometry data, we build our mathematical model so that it can be calibrated against this type of data. As shown in the schematic in Fig. 1, flow cytometry can distinguish cells in different stages of the cycle, sorting them according to their DNA content. While cells in the S phase are synthesising new DNA and, therefore, have a variable amount of DNA (from one to two copies), cells in the G1 and G2/M phases have exactly one and two copies of DNA, respectively. Although this method can fail to distinguish cells with similar DNA content (*i.e.*, cells in G1 and early S phases or, cells in the G2/M and late S phases), bromodeoxyuridine (BrdU) labelling can overcome this limitation. Since cells in the S phase incorporate BrdU into newly synthesised DNA, it is possible to distinguish these cells by measuring BrdU uptake (Ubezio, 2004). The bivariate distribution of cells over DNA content and BrdU labelling can therefore be used to estimate cell-cycle distributions which are usually presented as time series data for the evolution of the fractions of cells in the G1, S or G2/M phases. These estimates can be further refined by measuring the expression of proteins involved with cell-cycle regulation, such as cyclin-dependent kinases (Chiorino and Lupi, 2002; Ubezio, 2004).

Several mathematical formalisms have been proposed to investigate cell-cycle evolution in normal 'healthy' conditions, as well as perturbed environments, for example in the context of drug development. These formalisms encompass discrete (Fauré et al., 2006; Ubezio et al., 2009), continuous (either deterministic Alarcón et al., 2004; Basse et al., 2003; Basse et al., 2005; Fadda et al., 2012; Sasane, 2016; Simms et al., 2012; Sherer et al., 2008 or stochastic Altinok et al., 2011; Weber et al., 2014) and hybrid approaches (Alfieri et al., 2011; Singhania et al., 2011). When interested in the population scale, population balance (PB) models are often used (Basse et al., 2003; Basse et al., 2005; Fadda et al., 2012; Sasane, 2016; Sherer et al., 2008; Spinelli et al., 2006). These take the form of age- and/or phase-structured models, where a structure variable is introduced to track progress through the cell-cycle. Several recent reports have focused on developing compartment models of the cell-cycle, proliferation and migration which exploit time-resolved FUCCI data (Chao et al., 2017; Vittadello et al., 2018; Vittadello et al., 2019; Vittadello et al., 2021). When analysing flow cytometry data, instead, continuous structure variables are commonly used. For example, in a series of papers (Basse et al., 2003; Basse et al., 2004; Basse et al., 2005), Basse and coauthors developed cell-cycle models based on systems of partial differential equations in which cells are structured according to their DNA content. In these models, cells in the G1 and G2/M phases have constant DNA content (x), with $x = 1$ and $x = 2$, respectively, while x increases at a constant rate for cells in the S phase. Given a cell DNA content x at time t, and given its rate of DNA synthesis, it is possible to estimate the amount of time that a cell has spent in the S phase. However, information about the amount of time spent in the other phases of the cycle is lost. This shortcoming has motivated the development of age-structured models (Basse and Ubezio, 2007), in which the age of a cell in a certain phase of the cycle corresponds to the time it has spent in that phase. Models combining both structure variables (i.e., DNA and cell age) have also been proposed (Chapman et al., 2008), but they are complex and difficult to validate against data. Further cell-cycle specific properties such as size (Fadda et al., 2012), or protein expression levels (Chiorino and Lupi, 2002), can also be included in this framework. PB models can be extended to account for variability in compartment specific parameters, such as transition and/or death rates (Fadda et al., 2012) and length of cell-cycle phases (Basse et al., 2003), to capture the effect of different drugs on cell-cycle progression. Several theoretical studies have investigated the effect of chronic exposure to hypoxia on cell-cycle arrest (Alarcón et al., 2004; Csikász-Nagy, 2009) with particular emphasis on hypoxia-induced G1 arrest. At the population level, quiescence is usually represented by introducing an additional phase to the standard

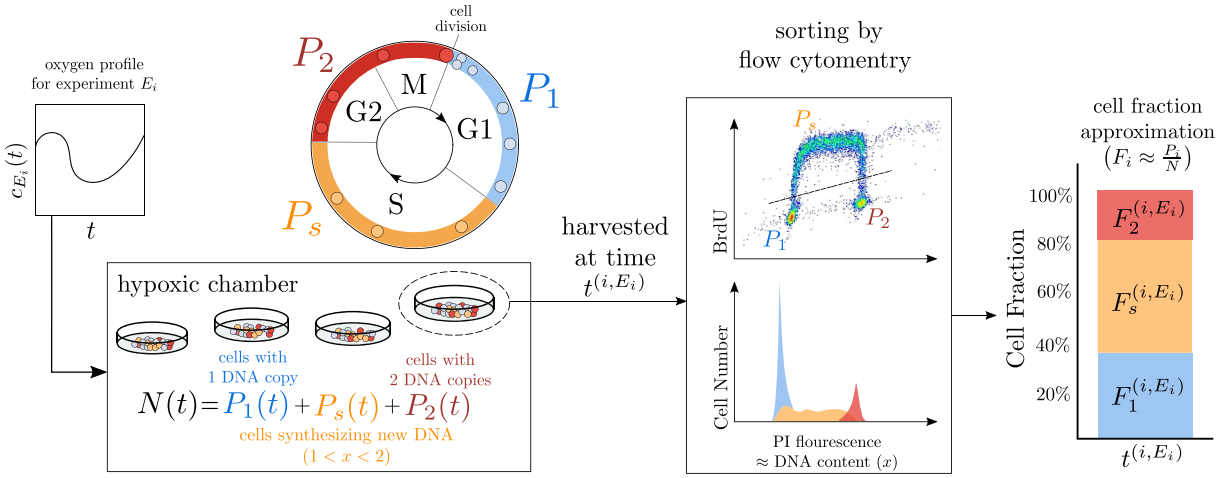

Fig. 1. Schematic representation of flow cytometric data: at different time points ($t^{(i,E_i)}$) during experiment E_i a subpopulation of N (the population of cells in the chamber) is harvested and sorted via flow cytometry according to their DNA content (PI fluorescence intensity), and BrdU uptake. This allows us to extract the fractions F_1, F_s and F_2 of cells in the subpopulation with one, intermediate (i.e. in between one and two), and two copies of DNA, respectively. This is an approximation of the frequency of cells with different DNA content in the total population in the chamber.

cell-cycle: the so-called 'G0' (or quiescent) phase (Ducrot et al., 2011; Gyllenberg and Webb, 1990), which cells enter prior to committing to DNA synthesis (i.e, prior to entering the S phase) when the local oxygen levels are too low ($\lessapprox 1\% O_2$). While this extension can account for cell responses to chronic hypoxia, recent experimental findings (Bader et al., 2021; Foskolou et al., 2017) suggest that this is not sufficient to account for cell behaviours in acute/-cyclic hypoxia.

In this paper we develop a mathematical model to investigate how periodic (rather than constant) RH influences cell-cycle dynamics. In §2 we introduce the experimental data from Bader et al. (2021) and summarise the biological mechanisms on which our model is based. In §3 we present our 6-compartment, DNA-structured, model which describes how the number of cells in each phase of the cycle evolves over time. Novel features of the model include a time- and oxygen-dependent rate of DNA synthesis (here denoted by $\nu(t)$) and the introduction of three "checkpoint" compartments ($C_1, C_2^{(a)}$ and $C_2^{(b)}$), where cells arrest due to unfavourable environmental conditions or due to the accumulation of damage and stress. We reduce our model to a system of 5 ordinary differential equations coupled to a delay-differential equation, where the delay (τ_S) represents the duration of the S phase and is not necessarily constant, rather, it depends on the environment that the cells have encountered. In §4, we first consider model predictions in well-oxygenated conditions. Here we recover the well-known result of cells converging to a regime of balanced exponential growth. In §5, we explore model predictions in constant and cyclic RH, highlighting the distinct effects that these two types of hypoxia have on the cell-cycle dynamics. We first show that the model can replicate experimental data from Bader et al. (2021) and then use it to investigate the cell-cycle dynamics for modes of oxygen fluctuations not yet tested experimentally. In §5.2, we introduce a class of models ($\mathscr{M}$) of decreasing complexity by neglecting some of the mechanisms (and complexity) included in the full model (such as arrest in $C_1, C_2^{(a)}$ and $C_2^{(b)}$). In §6 we compare these models using *Bayesian model selection*: we first calibrate our class of models against experimental data by using *Bayesian inference* methods and then identify the "best" model structure based on the *deviance information criteria*. This analysis reveals that the C_1 and $C_2^{(a)}$ checkpoint compartments are necessary to describe the experimentally observed dynamics. In §7, we use the selected and calibrated model to predict cell responses to different oxygen environments when considering the uncertainty in the parameter estimates. We also explain how our results could inform the design of new experiments to validate the model and/or improve the accuracy of the parameter estimates. In §8 we conclude by summarising our results and outlining possible directions for future work.

2. Experimental motivation

This work is inspired by experimental data showing how the cell-cycle of RKO (colorectal cancer) cells changes when they are cultured *in vitro* as 2D monolayers and exposed to fluctuating oxygen levels (Bader et al., 2021). As shown in Fig. 1, cells are cultured in chambers where the oxygen levels $c = c(t)$ (where t is time) are carefully controlled and assumed to be spatially homogeneous. At prescribed time points, a subset of the cells is analysed using flow cytometry to estimate the fractions of cells in the G1, S and G2/M phases of the cycle, which we denote, respectively, by F_1, F_s and F_2. Since each measurement requires cells to be harvested, measurement errors can be taken to be independent. In the absence of cell death, we have that by definition $F_1 + F_s + F_2 = 1$, so only two of the three cell fractions are needed to fully characterise the cell-cycle dynamics.

As shown in Fig. 2, two experimental protocols are tested. At time $t = 0$, cells are exposed to either constant radio-biological hypoxia ($c(t) \equiv c_{RH} \approx 0.1\% O_2, t > 0$) or periodic cycles of radio-biological hypoxia (2 hr at $c = c_{RH}$ and 2 hr at $2\% O_2$). Prior to both experiments, the cells are cultured in normoxia ($21\% O_2$) so that the measurements at time $t = 0$ contain information on this condition. In normoxia, and in absence of competition, the cells are typically in a regime of balanced exponential growth for which the cell fractions F_m are stationary (i.e., they do not change over time). Hence a single set of measurements is sufficient to fully characterise the cell-cycle dynamics in these environmental conditions. We divide the data into three different sets: E_0 (normoxia), E_1 (constant RH) and E_2 (cyclic RH). The histograms in Fig. 2 summarise the data available from Bader et al. (2021), obtained by averaging over multiple runs of the experiments. As mentioned in §1, our focus is on fluctuating environments (i.e. the scenario E_2), however data from E_0 and E_1 are also used to assist with parameter estimation.

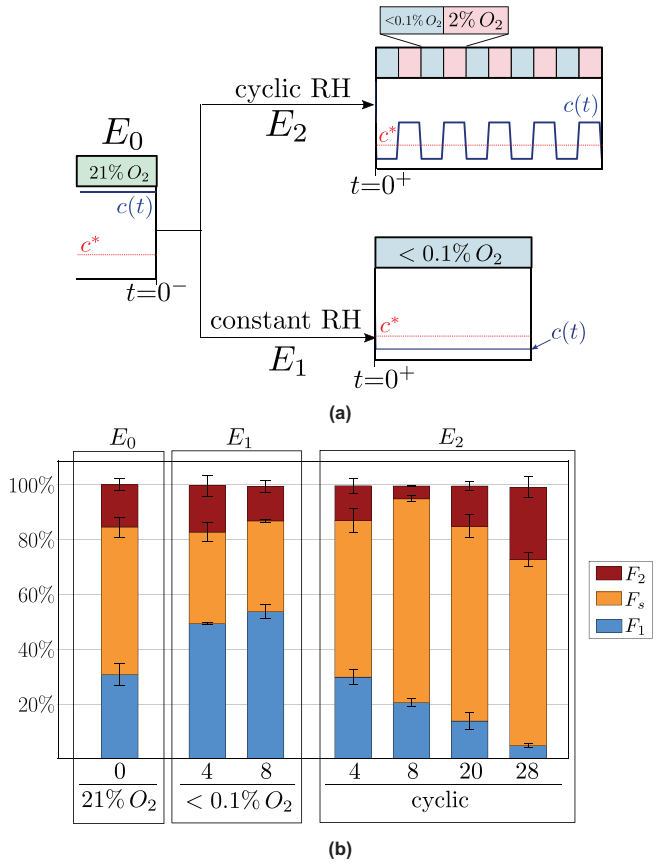

Fig. 2. (a) Data are split into three sets corresponding to the three experiments: normoxia (E_0), constant RH (E_1) and cyclic RH (E_2). We plot the evolution of the oxygen levels, $c(t)$ (see blue curve), and compare it to the threshold c^* at which DNA synthesis is impaired (see red horizontal line). (b) Histogram summarising the data from Bader et al. (2021). At each time point we report the mean cell fractions estimated from multiple (between two and four) measurements. Error bars indicate one standard deviation in the estimated values. The complete data sets can be found in Appendix B.

The data in Fig. 2 show that both constant (E_1) and cyclic RH (E_2) redistribute the cells along the cycle. For experiment E_1, cells tend to accumulate in the G1 phase (as seen by the increase in the fraction F_1), whereas in experiment E_2, we observe a decrease in the fraction F_1. In this case, cells initially concentrate in the S phase (as seen by the increase in the fraction F_s), while they accumulate in the G2/M phase at later times (see time $t = 28$ hr). For experiment E_1 we only consider the early dynamics since on longer time scales ($t > 20$ hr) cell-death becomes significant. By contrast, cells can survive for longer periods in cyclic hypoxia, with cell death being negligible for up to 28 hr.

As mentioned in the introduction, and based on current experimental evidence (Bader et al., 2021; Foskolou et al., 2017; Pires et al., 2010), three mechanisms may influence the cell-cycle dynamics under cyclic hypoxia: the reduction in the rate of DNA synthesis (Mechanism 1) and variation in the timing of the G1-S (Mechanism 2) transition, both due to dNTP shortage, and the arrest of cells in the G2 phase due to accumulation of damage and replication stress (Mechanism 3). Here, we assume that there is an oxygen threshold, c^*, such that dNTP levels drop (due to the impaired activity of RNR enzyme) when oxygen levels fall below c^*. We further hypothesise that cells experience transient mitotic arrest due to lack of oxygen (Mechanism 4). Based on the experiments in Foskolou et al. (2017), we estimate that $0.1\%O_2 < c^* < 2\%O_2$. We therefore fix c^* at an intermediate value (i.e., $c^* \approx 1\%O_2$). Our aim is to develop a mathematical model that captures these four mechanisms and that can be used to investigate whether they can explain the experimental data in both constant RH (E_1) and cyclic RH (E_2) conditions. Nonetheless, we can not exclude the possibility that other mechanisms (i.e., modelling assumptions) not considered here, might also explain the data.

3. The mathematical model

We propose a 6-compartment partial differential equation (PDE) model to describe cell-cycle dynamics in cyclic RH. For simplicity, we assume that the cells are in a well-mixed, spatially-homogeneous environment where the oxygen concentration $c = c(t)$ is externally prescribed. We also assume that cell death is negligible since this is supported by the experimental observations.

As illustrated in Fig. 3, we subdivide the population into 6 compartments. Here $G_1 = G_1(t)$ and $G_2 = G_2(t)$ denote, respectively, the number of cells at time t in the G1 and G2/M phases of the cycle that are actively proceeding along their cycle. On the other hand, $C_1 = C_1(t)$ and $C_2^{(b)} = C_2^{(b)}(t)$ are, respectively, the number of cells in the G1 and G2/M phases that are temporarily arrested at time t due to lack of oxygen. We denote by $C_2^{(a)} = C_2^{(a)}(t)$ cells that are arrested in G2 due to the damage and stress that they have accumulated during the S phase as a result of exposure to hypoxia. We view $C_1, C_2^{(a)}$ and $C_2^{(b)}$ as checkpoint compartments and assume that the rates of entry into, and exit from, these compartments change over time in response to current and previous environmental conditions (i.e, oxygen levels). Finally, we structure cells in the S phase according to their DNA content, x, so that $S = S(x,t)$ represents the number of cells with DNA content x at time t. Here x is a dimensionless variable corresponding to the relative DNA content of a cell, scaled so that $1 \leqslant x \leqslant 2$. Cells start the S phase with $x = 1$ and exit it upon completion of DNA duplication with $x = 2$.

Referring to the schematic in Fig. 3 and applying the principle of mass balance, we obtain the following system of equations for the time evolution of the model variables:

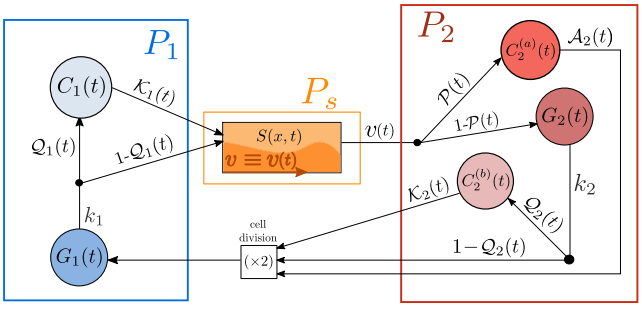

Fig. 3. Schematic representation of the 6-compartment model of the cell-cycle given by Eqs. (1). Here the two independent variables are time t and the cell DNA content x (measured in number of copies), while P_1, P_s and P_2 are as defined in Fig. 1. The sub-population P_1 groups cells in the G_1 and C_1 compartments, while P_2 comprises cells in the G_2, $C_2^{(a)}$ and $C_2^{(b)}$ compartments. Cells in the G compartments are progressing along the cell-cycle as usual, while the C compartments are "checkpoint" compartments where cells arrest. The black dots on the arrows correspond to redistribution of cell fluxes according to a given probability (for example in P_1 the influx $k_1 G_1$ is redistributed with probability Q_1 into C_1 and $1 - Q_1$ into S). To account for DNA synthesis during the S phase we structure cells in the S-compartment according to their DNA content x, which is synthesised at velocity v.

$$\frac{dG_1}{dt} = 2(k_2 G_2 + \mathscr{K}_2(t)C_2^{(b)} + \mathscr{A}_2(t)C_2^{(a)}) - k_1 G_1, \quad t > 0, \tag{1a}$$

$$\frac{dC_1}{dt} = Q_1(t)k_1 G_1 - \mathscr{K}_1(t)C_1, \quad t > 0, \tag{1b}$$

$$\frac{\partial S}{\partial t} + \frac{\partial}{\partial x}(v(t)S) = 0, \ x \in (1,2], \quad t > 0, \tag{1c}$$

$$\frac{dG_2}{dt} = -k_2 G_2 + (1 - \mathscr{P}(t))v(t)S(t,2), \quad t > 0, \tag{1d}$$

$$\frac{dC_2^{(a)}}{dt} = \mathscr{P}(t)v(t)S(t,2) - \mathscr{A}_2(t)C_2^{(a)}, \quad t > 0, \tag{1e}$$

$$\frac{dC_2^{(b)}}{dt} = Q_2(t)k_2 G_2 - \mathscr{K}_2(t)C_2^{(b)}, \quad t > 0. \tag{1f}$$

The factor of 2 in Eq. (1a) arises because cell division produces two daughter cells. The positive constants k_1, k_2 [hr^{-1}] represent the rates at which cells leave G_1, G_2, respectively. In Eq. (1c), we account for DNA synthesis by assuming that cells in the S compartment are advected along the x-axis at velocity $v(t) > 0$ [hr^{-1}] (i.e., they produce DNA at a rate $v(t)$). In Eq. (1b), we assume that cells exiting the G_1 compartment arrest (*i.e.* enter the C_1 compartment) with probability $Q_1 \in [0,1]$, while they proceed to enter the S phase with probability $1 - Q_1$. We further assume that arrested cells re-enter the cycle at rate $\mathscr{K}_1$ [hr^{-1}]. In a similar manner, in Eq. (1f) we assume that cells exiting the G_2 compartment (i.e., attempting mitosis) arrest in $C_2^{(b)}$ with probability $Q_2 \in [0,1]$, and re-enter the cycle at rate $\mathscr{K}_2$ [hr^{-1}]. Further we allow cells exiting the S phase to arrest due to damage with probability $\mathscr{P} \in [0,1]$. These damaged cells may re-enter the cycle at a rate $\mathscr{A}_2$. We account for the effect that different oxygen levels have on cell behaviour by allowing certain model parameters (specifically $\mathscr{K}_i, \mathscr{A}_2, v, \mathscr{P}$ and Q_i with $i = 1,2$) to vary over time in response to the oxygen levels c. The boundary condition for Eq. (1c) is derived by applying conservation of cell flux at $x = 1$. Under the assumption that $v(t) > 0$ for all $t > 0$, we find:

$$v(t)S(1,t) = (1 - Q_1(t))k_1 G_1(t) + \mathscr{K}_1(t)C_1(t). \tag{1g}$$

We close Eqs. (1a)–(1g) by imposing the following initial conditions:

$$\begin{aligned} &G_1(0) = G_{1,0}, \quad C_1(0) = C_{1,0}, \\ &S(x,0) = S_0(x) \ \ x \in (1,2], \\ &G_2(0) = G_{2,0}, \quad C_2^{(k)}(0) = C_{2,0}^{(k)}, \ \text{with } k \in \{a,b\}. \end{aligned} \tag{1h}$$

Since cell numbers can not be negative, in Eq. (1h) $G_{i,0}, C_{1,0}$ and $C_{2,0}^{(k)}$ are non-negative constants and $S_0(x)$ is a prescribed non-negative function $S_0(x) \geqslant 0$ for all $x \in [1,2]$.

In order to compare the model output to flow cytometry data, we need to express cell fractions (see Fig. 1) in terms of our model variables. As shown in Fig. 1, cells can be divided in three sub-populations depending on the cell-cycle phase they are in: P_1, P_s and P_2. Cells in G1 belong to P_1, cells in G2/M to P_2 and cells in S to P_s. The total number of cells, $N = N(t)$, is then obtained by summing the number of cells in each sub-population:

$$N(t) = P_1(t) + P_s(t) + P_2(t), \tag{2a}$$

where (as illustrated in Fig. 3),

$$\begin{aligned} P_1(t) &= C_1(t) + G_1(t), \\ P_s(t) &= \int_1^2 S(x,t)\,dx, \\ P_2(t) &= G_2(t) + C_2^{(a)}(t) + C_2^{(b)}(t). \end{aligned} \tag{2b}$$

Differentiating Eq. (2a) with respect to time and using (1), we find that $N(t)$ satisfies:

$$\frac{dN}{dt} = k_2 G_2 + \mathscr{K}_2(t)C_2^{(b)} + \mathscr{A}_2(t)C_2^{(a)}, \tag{3a}$$

$$\text{with} \quad N(0) = \sum_{i=1}^{2} G_{i,0} + C_{1,0} + \sum_{k\in\{a,b\}} C_{2,0}^{(k)} + \int_1^2 S_0(x)\,dx := N_0. \tag{3b}$$

The population proliferation rate, ω, is given by:

$$\omega(t) = \frac{1}{N}\frac{dN}{dt} = \frac{k_2 G_2 + \mathscr{K}_2(t)C_2^{(b)} + \mathscr{A}_2(t)C_2^{(a)}}{N}, \tag{4}$$

while the cell fractions f_m are defined by:

$$f_m(t) = \frac{P_m(t)}{N(t)}, \quad m \in \{1,s,2\}, \tag{5}$$

and correspond to the probability that a cell randomly chosen from the total population belongs to the sub-population P_m. We note that the fractions f_m are not independent; Eq. (2) implies that $\sum_m f_m = 1$. We further introduce the distribution $s = s(x,t)$:

$$s(x,t) = \frac{S(x,t)}{N(t)}, \quad 1 < x < 2, \tag{6}$$

which corresponds to the probability that a cell in the sub-population P_s has DNA content $x \in [1,2]$ at time t. A summary of the model variables is given in Table 1.

A key feature of our model is that the velocity v is assumed to depend on the oxygen levels c in order to account for impaired DNA synthesis at low oxygen levels ($c < c^*$). In particular, we propose the following piece-wise linear ODE to describe how the advection velocity v adapts to changes in local oxygen levels $c(t)$:

$$\frac{dv}{dt} = \begin{cases} -\mathscr{R}_-(v - v_-), & c(t) < c^*, \\ \mathscr{R}_+(v_+ - v), & c(t) \geqslant c^*, \end{cases} \tag{7a}$$

$$\text{with } v(0) = v_0. \tag{7b}$$

In Eqs. (7), $\mathscr{R}_\pm$, v_0 and $v_\pm$ are positive constants, while c^* is the threshold oxygen level below which RNR activity is impaired (see §2 for details). Here v_+ and v_- represent, respectively, the equilibrium velocities in well-oxygenated ($c > c^*$) and severely hypoxic ($c < c^*$) environments and $0 < v_- < v_+$. It is straightforward to show that if $v_0 \in [v_-, v_+]$, then $v(t) \in [v_-, v_+]$ at all times $t > 0$, so that v_+ and v_- can also be viewed, respectively, as the maximum and minimum rates of DNA synthesis. When oxygen levels drop below the critical value c^*, the rate of DNA synthesis decreases (i.e. $dv/dt \leq 0$ for $c < c^*$), capturing the effect of dNTP shortage. As observed in Foskolou et al. (2017), cells maintain a

Table 1
Summary of the model variables in Eqs. (1)-(8).

	Description
t	time [hr]
x	copies of DNA in a cell ($1.0 \leqslant x \leqslant 2.0$)
c	externally controlled oxygen levels [%]
$G_1(t)$	number of cells in P_1 active in the cycle
$C_1(t)$	number of cells in P_1 that are arrested in response to hypoxia
$S(x,t)$	number of cells in P_s with DNA content x
$G_2(t)$	number of cells in P_2 active in the cycle
$C_2^{(a)}(t)$	number of cells in P_2 that are arrested due to accumulation of damage and replication stress
$C_2^{(b)}(t)$	number of cells in P_2 that are arrested in response to hypoxia
$N(t)$	total cell number
$f_m(t)$	predicted fraction of cells ($f_m \in [0,1]$) in the P_m sub-population $m \in \{1,s,2\}$
$F_m(t)$	experimentally measured fraction of cells ($F_m \in [0,1]$) in the P_m sub-population $m \in \{1,s,2\}$
$s(x,t)$	DNA distribution of cells in the P_s sub-population
$\tau_S(t)$	duration of the S phase for cells that exit the S compartment at time t [hr]
$\omega(t)$	population proliferation rate [hr^{-1}]

minimum level of DNA synthesis even after prolonged exposure to severe hypoxia ($c < c^*$); we therefore assume that $v_- > 0$, which guarantees that $S(1,t)$, as defined by Eq. (1g), remains finite. Once $c > c^*$, dNTP levels are restored and the rate of DNA synthesis increases (i.e., $dv/dt > 0$) towards its maximum value v_+. The rates $\mathscr{R}_\pm$ are assumed constant for simplicity although, in practice, they may depend on oxygen levels. In the absence of suitable data to identify these dependencies, we proceed with the simplest form that captures the currently available data and postpone investigation of more complex functional forms to future work.

We introduce the checkpoint compartments C_1 and $C_2^{(b)}$ to account for transient arrest of cells in the P_1 and P_2 subpopulations, respectively, due to lack of oxygen. The rates of transition into (Q_i) and out of ($\mathscr{K}_i$) these compartments depend on current oxygen levels. For simplicity, we adopt the following functional forms to describe these rates:

$$\mathscr{K}_i(t) = K_i H_\epsilon(c(t) - c^*), \quad i \in \{1,2\}, \tag{8a}$$
$$Q_i(t) = q_i H_\epsilon(c^* - c(t)), \quad i \in \{1,2\} \tag{8b}$$

where K_i and q_i are non-negative constants with $q_i \in [0,1]$ and c^* is the oxygen threshold introduced above. The function H_ϵ is the standard continuous approximation of the Heaviside function:

$$H_\epsilon(\cdot) = \frac{1}{2}\left[\tanh\left(\frac{\cdot}{\epsilon}\right) + 1\right]. \tag{8c}$$

where $0 < \epsilon \ll 1$ is a small parameter, here set to $\epsilon = 0.01\%$ oxygen. We note that Eqs. (8a)-(8b) ensure that cells arrest when $c < c^*$ and resume cycling once $c > c^*$. We considered alternative functional forms for $\mathscr{K}_i$ and Q_i but found that the resulting model was unable to capture the experimentally observed dynamics (results not shown).

In Eq. (7), prolonged or frequent exposure to RH slows DNA replication and, therefore, increases the time τ_S that cells spend in the S phase. More precisely, we denote by $\tau_S = \tau_S(t)$ the amount of time a cell exiting the S phase at time t has taken to complete DNA synthesis (we will explain how $\tau_S(t)$ is computed in §3.1). Consequently, the larger τ_S, the more cells have been damaged during the S phase due to re-oxygenation and replication stress (in RH). Since the accumulation of damage in the S phase regulates the following arrest of cells in the G2 phase (here captured by cells transitioning into the $C_2^{(a)}$ compartment), we assume that the probability, $\mathscr{P}(t)$, of arrest in G2 increases with $\tau_S(t)$. In particular, we assume that, when cells exit the S phase, they arrest with a probability $\mathscr{P} \in [0,1]$ where:

$$\mathscr{P}(t) = pH_{\epsilon_p}(\tau_S(t) - T). \tag{8d}$$

In Eq. (8d), we fix the small parameter ϵ_p so that $\epsilon_p = 0.1$ hr, while $p \in [0,1]$ and $T > 0$ are unknown parameters. Here p is the maximum probability that a cell enters the $C_2^{(a)}$ compartment while T captures the critical duration of the S phase after which cells are likely to arrest in $C_2^{(a)}$. Based on Eq. (7), the timescale for completing the S phase, τ_S, satisfies $v_+^{-1} \leqslant \tau_S \leqslant v_-^{-1}$. When oxygen levels are sufficiently high, (i.e. $c(t) > c^*$ for all t), neglecting an initial transient in the case $v_0 \neq v_+$, we have that $\tau_S \equiv v_+^{-1}$. Since we do not expect cells to arrest in an oxygen-rich environment we require $\mathscr{P}(t) \approx 0$ when $\tau_S(t) \equiv v_+^{-1}$. Consequently we set $T \gg v_+^{-1}$. As in Eq. (8a), we assume that, once oxygen levels rise above the critical value c^*, cells can repair any damage they have accumulated and re-enter the cell-cycle at a rate $\mathscr{A}_2$:

$$\mathscr{A}_2(t) = \alpha_2 H_\epsilon(c(t) - c^*), \tag{8e}$$

where α_2 is a non-negative constant and $\epsilon = 0.01\%$ oxygen as in Eq. (8a).

3.1. Model reduction to a system of Delay Differential Equations (DDEs)

Here we show how Eqs. (1) can be rewritten as a system of ODEs coupled to a (state-dependent) DDE with a non-constant delay $\tau_S(t)$ which we view as a state variable. Given that the velocity v is always positive, shocks can not form and a straightforward application of the *method of characteristics* to Eq. (1c) yields

$$S(x,t) = \begin{cases} S_0\left(x - \int_0^t v(\ell)d\ell\right), & \int_0^t v(\ell)d\ell \leqslant x-1, \\ \frac{(1-Q_1)k_1G_1 + \mathscr{K}_1 C_1}{v}\big|_{t-\tau(t,x)}, & \int_0^t v(\ell)d\ell > x-1, \end{cases} \tag{9}$$

where the function $\tau = \tau(t,x)$ is implicitly defined by:

$$x - 1 = \int_{t-\tau(t,x)}^t v(\ell)d\ell, \qquad \text{if } \int_0^t v(\ell)d\ell > x-1, \tag{10}$$

and indicates the amount of time a cell with DNA content x at time t has spent in the S compartment.

As illustrated in Fig. 4, the condition $\int_0^t v(\ell)d\ell = x-1$ divides the (t,x)-plane into two regions depending on whether the characteristics propagate from the boundary data curve (orange curve) or the initial data curve (green curve). When $t > t^*$ (i.e. when $S(2,t)$ is influenced by the boundary data) the total time spent in the S compartment is given by $\tau_S(t) = \tau(t,2)$. Using Eq. (10), we find that τ_S is implicitly defined by:

$$1 = \int_{t-\tau_S(t)}^t v(\ell)d\ell, \quad \text{if } t > t^*, \tag{11a}$$

where t^* is defined implicitly by the integral equation

$$\int_0^{t^*} v(\ell)d\ell = 1. \tag{11b}$$

However, more information about the behaviour of cells prior to the beginning of the experiment is needed to estimate $\tau_S(t)$ for $0 \leqslant t < t^*$. Let us consider a cell that exits the S phase at time $t < t^*$. Then, at time $t = 0$, its DNA content was:

$$x_0(t) = 2 - \int_0^t v(\ell)d\ell, \tag{12}$$

as we can write $\tau_S = t + \tau_0$, where t denotes the time spent in the S compartment since the beginning of the experiment and τ_0 the time spent in the S phase prior to the beginning of the experiment. The functional form of τ_0 will depend on the conditions in which the cells were grown for $t < 0$. It is therefore part of the initial data that

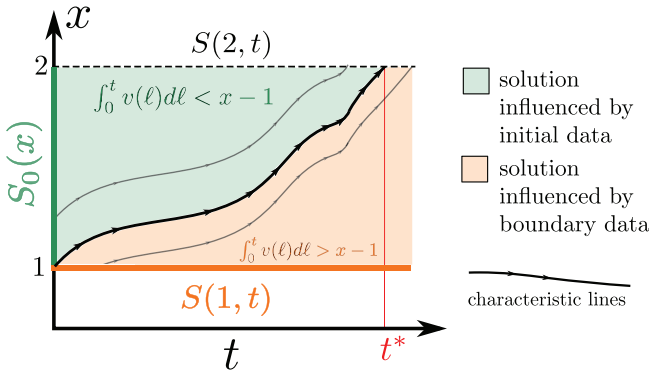

Fig. 4. Schematic illustration of the characteristic curves in the (t,x) plane. The bold curve divides the plane into two distinct regions: in the green region (where $\int_0^t v(\ell)d\ell < x-1$) the solution $S(x,t)$ is determined by the initial data; in the orange region (where $\int_0^t v(\ell)d\ell > x-1$) $S(x,t)$ is instead determined by the boundary data.

must be specified in order to fully define the model. In §4, we will show that if cells are cultured in an oxygen-rich environment for $t<0$, then τ_0 depends only on the DNA content $x_0(t)$ (*i.e.* $\tau_0(t)=\tau_0(x_0(t))$). In summary we have:

$$\tau_S(t)=t+\tau_0(t),\quad 0\leqslant t<t^*. \tag{13}$$

Differentiating Eq. (11a) with respect to time, and given Eq. (13), we deduce that the variable $\tau_S(t)$ satisfies:

$$\frac{d\tau_S}{dt}=1-\frac{v(t)}{v(t-\tau_S)},\quad t\geqslant t^*, \tag{14a}$$

$$\text{with } \tau_S(t)=t+\tau_0(t),\quad 0\leqslant t\leqslant t^*. \tag{14b}$$

3.2. Summary of the cell-cycle model with delay

Before presenting the full model, we perform the following re-scaling:

$$\widehat{G}_i=\frac{G_i}{N_0},\quad \widehat{C}_1=\frac{C_1}{N_0},\quad \widehat{C}_2^{(k)}=\frac{C_2^{(k)}}{N_0},\quad \widehat{N}=\frac{N}{N_0}. \tag{15}$$

Since our model is linear, this re-scaling does not affect the form of the governing equations; it only alters the initial conditions. We further assume that cells are initially actively cycling (*i.e.* none of them is arrested) and DNA synthesis is proceeding at maximum speed so that:

$$v_0=v_+,\quad C_{1,0}=0,\quad C_{2,0}^{(k)}=0,\quad f_{i,0}=\frac{G_{i,0}}{N_0},\quad i\in\{1,2\}, \tag{16}$$

where $f_{i,0}$, with $i\in\{1,2\}$, denote the cell fractions at time $t=0$. As discussed in §4, this is a reasonable assumption if cells are cultured in oxygen-rich environments prior to the start of the experiments.

Applying Eq. (15) to Eqs. (1)–(3), using Eqs. (7)–(8), (9) and (14) and dropping the hat notation, the governing equations become

$$\frac{dG_1}{dt}=2(k_2G_2+\mathscr{K}_2(t)C_2^{(b)}+\mathscr{A}_2(t)C_2^{(a)})-k_1G_1,\quad t>0, \tag{17a}$$

$$\frac{dC_1}{dt}=Q_1(t)k_1G_1-\mathscr{K}_1(t)C_1,\quad t>0, \tag{17b}$$

$$\frac{dG_2}{dt}=-k_2G_2+(1-\mathscr{P}(t))\,I(t-\tau_S(t),t)\quad t>0, \tag{17c}$$

$$\frac{dC_2^{(a)}}{dt}=\mathscr{P}(t)I(t-\tau_S(t),t)-\mathscr{A}_2(t)C_2^{(a)},\quad t>0, \tag{17d}$$

$$\frac{dC_2^{(b)}}{dt}=Q_2(t)k_2G_2-\mathscr{K}_2(t)C_2^{(b)},\quad t>0, \tag{17e}$$

$$\frac{dN}{dt}=k_2G_2+\mathscr{K}_2(t)C_2^{(b)}+\mathscr{A}_2(t)C_2^{(a)},\quad t>0, \tag{17f}$$

$$\frac{dv}{dt}=\begin{cases}-\mathscr{R}_-(v-v_-), & c(t)<c^*,\\ \mathscr{R}_+(v_+-v), & c(t)\geqslant c^*,\end{cases}\quad t>0, \tag{17g}$$

$$\frac{d\tau_S}{dt}=\frac{v(t-\tau_S)-v(t)}{v(t-\tau_S)},\quad t\geqslant t^* \tag{17h}$$

wherein t^* is implicitly defined by Eq. (11b) and

$$I(s,t)=\begin{cases}v(t)s_0\left(2-\int_0^t v(\ell)d\ell\right), & t<t^*,\\ v(t)\frac{(1-Q_1(s))k_1G_1(s)+\mathscr{K}_1(s)C_1(s)}{v(s)}, & t\geqslant t^*,\end{cases} \tag{17i}$$

$$\mathscr{K}_i(t)=K_iH_\epsilon(c(t)-c^*),\quad i\in\{1,2\}, \tag{17j}$$

$$\mathscr{A}_2(t)=\alpha_2H_\epsilon(c(t)-c^*), \tag{17k}$$

$$Q_i(t)=q_iH_\epsilon(c^*-c(t)),\quad i\in\{1,2\} \tag{17l}$$

$$\mathscr{P}(t)=pH_{\epsilon_p}(\tau_S(t)-T), \tag{17m}$$

and

$$\begin{aligned}&v(0)=v_+,\quad \tau_S(\xi)=\xi+\tau_0(\xi), && 0\leqslant\xi\leqslant t^*,\\ &N(0)=1,\quad C_1(0)=0,\\ &G_i(0)=f_{i,0},\quad C_2^{(k)}(0)=0, && k\in\{a,b\}.\end{aligned} \tag{17n}$$

In Eq. (17c), $I(t-\tau_s(t),t)$ denotes the flux of cells exiting the S compartment at time t, i.e., $I(t-\tau_s(t),t)=v(t)S(2,t)$ where S satisfies Eq. (9). To close the system, it remains to specify the distribution $s_0(x)=s(x,t=0)=S_0/N_0$ and the function τ_0 (see §3.1). The former is subject to the constraint:

$$\int_1^2 s_0(x)\,dx=f_{s,0}=1-f_{1,0}-f_{2,0}. \tag{18}$$

In Fig. 5, we present a schematic summary of the model (as in Fig. 3) where the S compartment is replaced by the time delay τ_S.

As listed in Table 2, our model has 12 parameters. As discussed in §2, we fix $c^*=1\%$ oxygen in line with experimental evidence. Further, based on the experimental estimates of the rate of DNA synthesis in Pires et al. (2010), we expect v_- to be small. Since the limit $v_-\to 0$ is non-singular, it can be shown that the solution is not sensitive to the precise value of v_- provided that $v_-\sim O(10^{-3})$ (results not shown). We therefore fix $v_-=0.005\,\mathrm{hr}^{-1}$, which is sufficiently small to exhibit the correct qualitative behaviour. With $c^*=1$ and $v_-=0.005$, there are ten unknown parameters, which we split into two classes. While $\boldsymbol{\theta}=[k_1,v_+,k_2]$ comprises parameters associated with oxygen-independent mechanisms, $\boldsymbol{\Theta}=[\mathscr{R}_+,\mathscr{R}_-,K_1,q_1,p,T,\alpha_2,K_2,q_2]$ contains parameters associated with oxygen-dependent mechanisms. Given the large number of unknown parameters and the expected variability for different cell lines, we here focus on the RKO cancer cell line and the data in Fig. 2 to estimate the model parameters. Discussion on how we estimate the model parameters is postponed to §6. First, we present some characteristic predictions of our model obtained by solving Eqs. (17) numerically using the Python *ddeint* package to integrate delay-differential equations.

4. Cell-cycle progression in a static normoxic environment

Let us first consider the case in which cells are exposed to a constant, oxygen-rich environment (i.e., $c(t)\equiv\bar{c}\gg c^*$). Given Eqs. (17g)-(17h), we have that $v\equiv v_+$ and $\tau_S\equiv v_+^{-1}$. In this case, $Q_i\equiv 0$, $\mathscr{P}\equiv 0$ and $C_1(t)=C_2^{(a)}(t)=C_2^{(b)}(t)\equiv 0$ for all $t>0$, so that there are no arrested cells in the population. We conclude that when $c\equiv\bar{c}>c^*$, Eqs. (17) reduce to the following system:

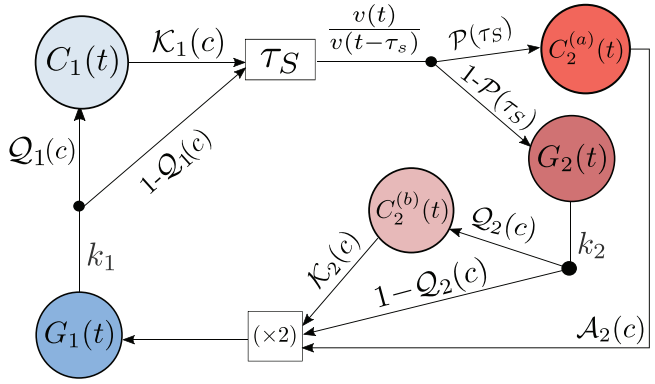

Fig. 5. Schematic representation of the 5-compartment model with delay (see Eqs. (17)) derived by solving Eq. (1) via the method of characteristics. The black nodes correspond to the conservation of the cell fluxes, where the input is redistributed with probabilities $P(\tau_S)$ $(Q_i(c), i=1,2)$ and $1-P(\tau_S)$ $(1-Q_i(c))$ in $C_2^{(a)}$ $(C_1/C_2^{(b)})$ and G_2 ("delay" compartment τ_S/G_1.), respectively.

Table 2
Summary of the parameters that appear in Eqs. (1)–(8), together with their typical values for the RKO cancer cell line.

	Description	Typical value (s)
c^*	oxygen tension at which RNR activity is impaired leading to dNTP shortage	$\approx 1\% O_2$
v_-	minimum velocity of DNA synthesis	5×10^{-3} hr^{-1}
v_+	maximum velocity of DNA synthesis	0.083 hr^{-1}
k_1	rate at which cells exit G_1	0.195 hr^{-1}
k_2	rate at which cells exit G_2	0.22 hr^{-1}
K_1	rate at which cells leave C_1	0.0 – 2.5 hr^{-1}
q_1	probability of a cell arresting in C_1 in RH	0.0 – 1.0
α_2	rate at which damaged cells leave $C_2^{(a)}$	0.0–2.0 hr^{-1}
T	threshold for transition to $C_2^{(a)}$ checkpoint	15 – 20 hr
p	maximum probability of a cell arresting in $C_2^{(a)}$	0.0 – 1.0
K_2	rate at which cells leave $C_2^{(b)}$	0.0 – 2.5 hr^{-1}
q_2	probability of a cell arresting in $C_2^{(b)}$ in RH	0.0 – 1.0
$\mathscr{R}_+$	rate of change of v when $c > c^*$	10^{-3} – 2.0 hr^{-1}
$\mathscr{R}_-$	rate of change of v when $c < c^*$	10^{-3} – 2.0 hr^{-1}

$$\frac{dG_1}{dt} = 2k_2G_2 - k_1G_1, \quad t > 0, \tag{19a}$$

$$\frac{dG_2}{dt} = -k_2G_2 + k_1G_1(t - v_+^{-1}), \quad t > 0, \tag{19b}$$

$$\frac{dN}{dt} = k_2G_2, \quad t > 0, \tag{19c}$$

subject to

$$G_1(\xi) = \begin{cases} f_{1,0}, & \xi = 0, \\ v_+k_1^{-1}s_0(2 + \xi v_+), & -v_+^{-1} < \xi < 0, \end{cases} \tag{19d}$$
$$N(0) = 1, \quad G_2(0) = f_{2,0},$$

where s_0 satisfies Eq. (18).

We note that Eqs. (19) are analogous to models previously proposed in the literature, such as the model by Basse et al. (Basse et al., 2003; Basse et al., 2004) when dispersion is neglected. Since Eqs. (19) are linear with a constant delay, they can be solved exactly via superposition of exponential functions $e^{\Lambda_i t}$ where Λ_i $(i = 1, 2, \ldots)$ are the complex roots of the characteristic polynomial (see Eq. (A.3) in Appendix A). In the case of DDEs, the characteristic polynomial is a transcendental equation with an infinite number of roots so that the computation of Λ_i is non-trivial. To investigate the transient dynamics, it is therefore more convenient to solve Eqs. (19) numerically. In Fig. 6 we present numerical solutions for two sets of initial conditions: cells are initially synchronised in either the G_1 (Fig. 6(a)) or G_2 (Fig. 6(b)) compartment. This corresponds to setting $s_0 \equiv 0$ with $f_{1,0} = 1$ and $f_{2,0} = 0$ (for panel (a)), or $f_{2,0} = 1$ and $f_{1,0} = 0$ (for panel (b)).

As shown in Fig. 6, the evolution of the cell fractions f_m in panels (a.1) and (b.1) differs only up to time $t \approx 20$ hr; after this first transient the cell fractions evolve to constant values, denoted by $\bar{f}_m$, which are independent of the initial conditions. When looking at Fig. 6(a.2)-(b.2), we see that, from time $t > 20$ hr, the variables have a similar qualitative behaviour, but their values remain higher for scenario (b) than for scenario (a). While cells in scenario (b) start proliferating at the beginning of the simulations, cells in scenario (a) are delayed since they need to complete the S phase before they can replicate. Once cells enter the G_2 compartment, we see an increase in the cell number N. We also note that from time $t > 60$ hr, for both scenarios, $N(t), G_1(t)$ and $G_2(t)$ increase exponentially at a constant rate. This agrees with the results in Fig. 7, which show that the population proliferation rate $\omega(t)$

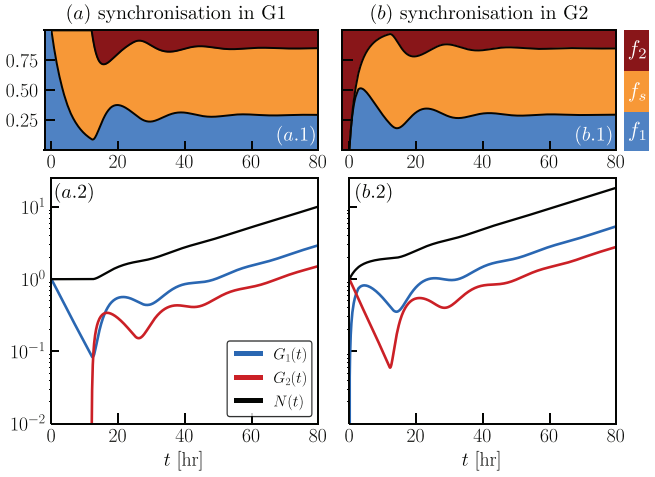

Fig. 6. Numerical simulations of Eqs. (19) for two sets of initial conditions: (a) $s_0 \equiv 0$, $f_{2,0} \equiv 0$ and $f_{1,0} = 1$; (b) $s_0 \equiv 0$, $f_{2,0} \equiv 1$ and $f_{1,0} = 0$. For both simulations, the parameters k_1, k_2 and v_+ are set as in Table 2. In panels (a.1) and (b.1), we plot the cell-cycle dynamics with cumulative plots of the cell fractions f_m with $m \in \{1, s, 2\}$; in panels (a.2) and (b.2) we show instead the predicted time evolution of the model variables G_1, G_2 and N on a semi-logarithmic scale.

(see Eq. (4)) asymptotes to a constant value λ for both sets of simulations.

Fig. 8 shows the evolution of the distribution $s(x, t)$. We note that in Fig. 8(a), cells are initially highly synchronised in the S compartment, with the formation of a front that propagates at velocity v_+ (note the steep gradient in the profiles at times $t = 5$ and $t = 10$). This is because of the discontinuity in the initial data for G_1 (when $f_{1,0} = 1$ and $S_0 \equiv 0, G_1(\xi)$ in Eqs. (19) is discontinuous at $\xi = 0$). The discontinuity propagates along the x axis but it quickly smooths out due to the de-synchronisation of cells in the G_1 and G_2 compartments. By contrast, in Fig. 8(b), there is no discontinuity in the initial data for G_1 and therefore the profile of s is smoother. Despite these large differences in the distributions at early times, s eventually evolves to the same stationary distribution (in Fig. 8, the curves for $t = 60$ and $t = 80$ are almost indistinguishable) and the time scales required to approach the stationary distribution for the two initial conditions are comparable.

Following the notation introduced in Simms et al. (2012), we term the asymptotic solution of the reduced model (19) a *phase stationary solution* (PSS) to indicate that, in this regime, the cell fractions f_1, f_s and f_2, and the distribution s remain constant in time. This is similar to predictions from other models in the literature (Basse et al., 2003; Basse et al., 2005; Begg et al., 2008; Crivelli et al., 2012; Simms et al., 2012) in the context of unperturbed growth; this regime is usually referred to as balanced, or

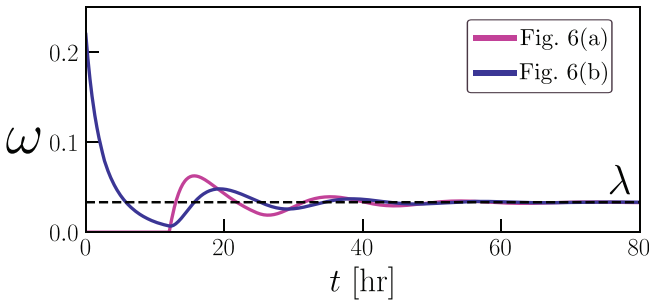

Fig. 7. Comparison of the population proliferation rate ω (see Eq. (4)) for the two scenarios in Fig. 6. We see that on the long time scale, the proliferation rate settles to a constant value, λ, independently of the initial conditions chosen.

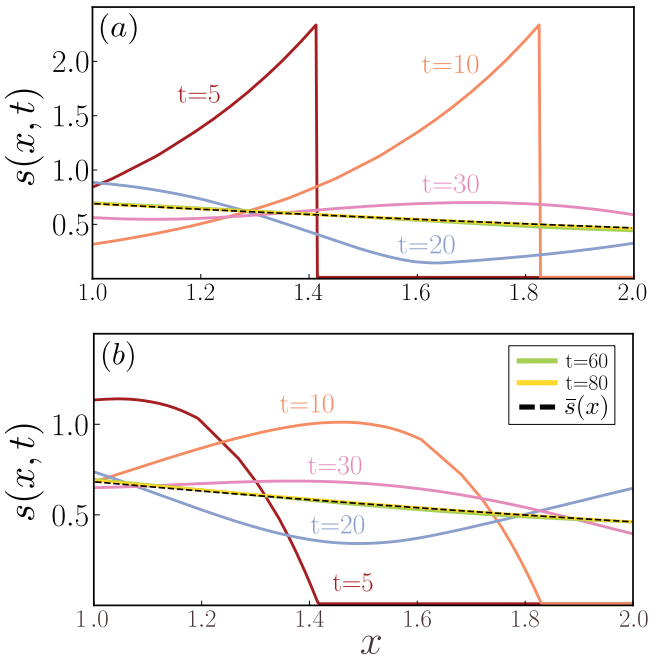

Fig. 8. Evolution of the distribution of cells in the S compartment with respect to x. We estimate the distribution $s(x,t)$ by numerically solving Eq. (9) for the two cases in Fig. 6: (a) initial synchronisation in G_1 (as in Fig. 6a) and (b) initial synchronisation in G_2 (as in Fig. 6b). We compare the long time behaviour with the analytically computed solution from the phase stationary solution $\bar{s}(x)$ (see black dashed line). Here the colour scheme in (a) and (b) is the same.

asynchronous, exponential growth (Basse et al., 2004; Bell, 1968). As mentioned previously, we can write the solution to Eqs. (19) as a superposition of exponential functions $e^{\Lambda_i t}$. At long times, the behaviour is dominated by the exponential whose eigenvalue Λ_i has the largest real part (here denoted by λ). It is possible to prove that this eigenvalue λ is real and positive (see Appendix A for details). We conclude that for $t \gg 1$ the system approaches a regime of exponential growth (as observed in the numerical results in Fig. 6) in which the model variables take the form:

$$\begin{aligned} &G_{1,2}(t) \approx \bar{f}_{1,2}\,\xi_N e^{\lambda t}, \\ &N(t) \approx \xi_N e^{\lambda t}, \qquad\qquad t \gg 1. \\ &S(x,t) \approx k_1 \bar{f}_1\, v_+^{-1} e^{-\lambda v_+^{-1}(x-1)} \xi_N e^{\lambda t}, \end{aligned} \tag{20}$$

where $\bar{f}_{1,2} \geqslant 0$ and $\xi_N > 0$ are constant. Substituting Eqs. (20) into Eqs. (5), we obtain that for $t \gg 1$, $f_m(t) \to \bar{f}_m$ for $m \in \{1, s, 2\}$. Therefore $\bar{f}_1$, $\bar{f}_s$ and $\bar{f}_2$ indicate, respectively, the stationary values of cell fractions in the G1, S and G2/M phases of the cycle. The distribution of cells, $s(x,t)$, converges to the stationary distribution $\bar{s}(x) = v_+^{-1} k_1 \bar{f}_1 e^{-\lambda v_+^{-1}(x-1)}$, which is monotonically decreasing in x (see black dashed line in Fig. 8). This indicates that, for $t \gg 1$, cells in S phase are more likely to be starting DNA synthesis (with $x \approx 1$) rather than close to completing it (with $x \approx 2$). We note that the longer the duration of the S phase, or equivalently the smaller v_+, the steeper is the $\bar{s}(x)$ curve and, therefore, the larger is the number of cells in P_s that are concentrated around $x \approx 1$. In the limit where the population growth rate λ is much smaller than the rate of DNA synthesis, i.e. $\lambda v_+^{-1} \to 0$, the distribution $\bar{s}(x)$ flattens and cells are distributed uniformly throughout the S phase.

We remark that balanced exponential growth is valid when non-linear effects (due to competition) can be neglected. This is the case in the given experimental settings where cells are grown in a nutrient-rich environment in the absence of contact inhibition (Basse et al., 2003; Simms et al., 2012).

5. Cell-cycle progression in a dynamic environment

Having discussed the model predictions for a well-oxygenated environment, we now investigate the behaviour it exhibits under radio-biological hypoxia (RH). We start by comparing how continuous (E_1) and cyclic RH (E_2) affect RKO cells originally in a regime of exponential growth (i.e., the phase stationary solution computed in §4). To replicate the oxygen dynamics in the experiments from Bader et al. (2021), we use the following functional form for the oxygen levels $c = c(t)$ at time $t > 0$:

$$c(t) = c_+ + (c_+ - c_{RH}) \sum_{i=1} \left[H_\epsilon(t - t_i^{(R)}) - H_\epsilon(t - t_i^{(H)}) \right], \tag{21}$$

where H_ϵ is defined in Eq. (8c), $t_i^{(H)}$ and $t_i^{(R)}$ are the times at which oxygen levels decrease and increase across the threshold $c = c^*$, respectively. By fixing $t_i^{(R)} = 4(i-1)+2$ and $t_i^{(H)} = 4(i-1)$, $c_{RH} \approx 0.1\%$ oxygen and $c_+ = 2\%$ oxygen, we can reproduce the 2hr + 2hr cycle corresponding to experiment E_2 in Fig. 2. Fixing $t_1^{(H)} = 0$ and $t_1^{(R)} = \infty$, we obtain the constant RH (E_1) conditions with $c < c^*$ for $t > 0$.

Initial conditions. Under standard culture conditions, cells *in vitro* are typically in a regime of balanced growth. We therefore initiate our simulations by assuming that cells are growing according to Eqs. (20). Recalling that we have re-scaled the model so that $N(0) = 1$, we have the following initial conditions:

$$\begin{aligned} &G_1(0) = \bar{f}_1, \quad s_0(x) = \tau_s k_1 \bar{f}_1 e^{-\lambda \tau_s (x-1)}, \\ &G_2(0) = \bar{f}_2, \quad C_1(0) = 0, \quad C_2^{(k)}(0) = 0. \end{aligned} \tag{22a}$$

Finally, to complete Eqs. (14), we must specify the function τ_0 (see §3.1). Since we assume DNA is synthesised at a constant rate v_+ for $t < 0$, it is straightforward to show that cells with DNA content x at time $t = 0$ have spent a period $\tau_0(s) = \frac{s-1}{v_+}$ in the S phase. Using Eq. (12), we have that

$$\tau_0(t) = \frac{1}{v_+} \left(1 - \int_0^t v(\ell) d\ell \right), \quad t \leqslant 0. \tag{22b}$$

5.1. Numerical results

We start by considering scenario E_1 where cells are exposed to constant RH for about 15 hr (see Fig. 9a and pink curve in Fig. 10). As mentioned in §2, at longer times, cells start dying and our model stops being valid, therefore we run simulations only up to this time. Fig. 10(a.1) shows that $f_1(t)$ rapidly increases in the first 5 h, while it appears to settle to a value of $\approx 50\%$ at longer times. This suggests that cells tend to accumulate in the G1 phase. By contrast, both $f_s(t)$ and $f_2(t)$ decrease. While $f_s(t)$ decreases monotonically over time, the decrease in $f_2(t)$ is delayed by a couple of hours, during which time its value remains approximately constant. Focusing now on the evolution of the number of cells in each model compartment (see Fig. 9(a.3)), we see that the number of cells in the C_1 compartment increases monotonically, but the rate of increase tends to slow after about 10 h. By contrast, $G_1(t)$ slightly increases in the first few hours (≈ 4 hr) while it decreases rapidly at later times. Similarly, the G_2 compartment starts to empty only after a couple of hours from the beginning of the simulation (see Fig. 10(a.2)). As the velocity v decreases (see Fig. 10(b)), the flux of cells out of the S phase (see Eqs. (17)) also decreases, contributing to the reduction in $G_2(t)$. The number of cells in $C_2^{(b)}$ increases over time as expected; however the accumulation of arrested cells in $C_2^{(b)}$ is negligible when compared to the large increase in $C_1(t)$. Even though τ_S quickly increases above the threshold $T \approx 17$ (see Fig. 10(d)), very few cells accumulate in $C_2^{(a)}$. They, instead, remain

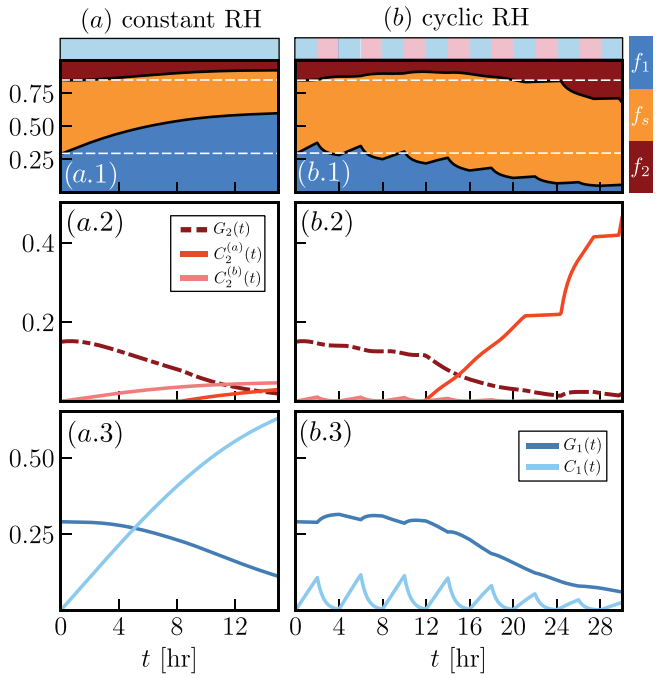

Fig. 9. Numerical simulations of cell-cycle evolution as predicted by Eqs. (17) and (21)–(22) in constant RH (a) and cyclic RH (b). The top row illustrates the evolution of the oxygen levels c in the two simulations, where the light blue and red areas indicate, respectively, the times at which $c < c^*$ and $c > c^*$. The cell-cycle dynamics are shown in the middle row panels where we plot the evolution of cell fractions over time in the form of a cumulative diagram. The white lines indicate the composition at time $t = 0$, i.e., the phase stationary solution $\bar{f}_1, \bar{f}_s$ and $\bar{f}_2$. Panels (a.2) and (b.2) show the predicted evolution of cell numbers for the model compartments contained within the P_2 phase: $G_2(t)$, $C_2^{(a)}(t)$ and $C_2^{(b)}(t)$. Panels (a.3) and (b.3) show the predicted evolution of cell numbers for the model compartments contained within the P_1 phase: $G_1(t)$ and $C_1(t)$. The parameters $k_1, v_\pm$ and k_2 are as in Table 2 while the remaining parameter values are the estimated mean parameter values for model $\mathscr{M}_0$ reported in Table C.9.

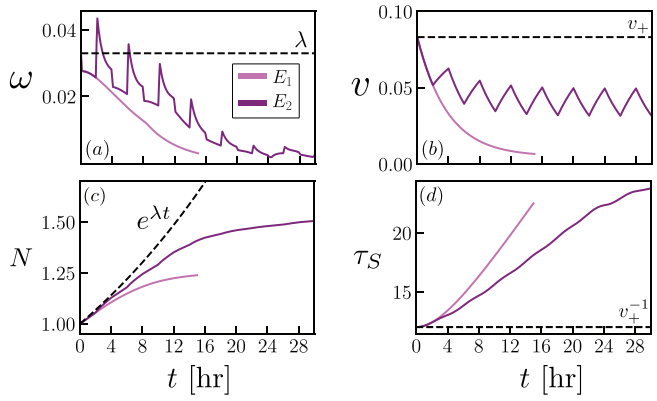

Fig. 10. We compare the predicted population dynamics for the two simulations in Fig. 9: (a) population proliferation rate ω as defined by Eq. (4), (b) the total cell number N, (c) the DNA synthesis velocity v and (d) the duration of the S phase τ_S. The parameters are chosen as in Fig. 9.

trapped in the S phase due to the reduction in the rate of DNA synthesis. Given $G_2(t)$, the activation of the $C_2^{(a)}$, $C_2^{(b)}$checkpoint compartments, the overall proliferation rate decreases monotonically (see Fig. 10)) and drives the gradual flattening of the population growth curve for $N(t)$ (see Fig. 10(c)). Note that the steep decrease in ω at time $t = 0$ in Fig. 10(a) is due to the rapid activation of the $C_2^{(b)}$ checkpoint.

In the case of cyclic RH (E_2), the dynamics are quite different. As shown in Fig. 9(b), while initially $f_s(t)$ increases and $f_2(t)$ decreases, the opposite occurs at later times ($t \approx 25$ hr) when $f_2(t)$ increases while $f_1(t)$ decreases. Overall, the fraction $f_1(t)$ decreases, albeit non-monotonically, so that, at the end of the simulation, its value is almost negligible (i.e., $0 < f_1 \ll 1$). Looking at the evolution of the number of cells in each compartment illustrated in Fig. 9(b.2)-(b.3), we see that cells transiently accumulate in the C_1 compartment during exposure to RH (light blue curve) and resume cycling during re-oxygenation. A similar trend is observed for $C_2^{(b)}$ but the number of cells that accumulate is negligible. The evolution of G_2 and G_1 is qualitatively similar; both remain approximately constant up to $t \approx 15$ hr, after which time they start to decrease. At the same time, the $C_2^{(a)}$ checkpoint is activated (Fig. 10(d) shows that $\tau_S(t) \approx T = 17.03$ hr so that $P \approx p/2$ for $t \approx 15$ hr). Since the $C_2^{(a)}$ checkpoint prevents cells from replicating, its activation results in a rapid decrease in the population proliferation rate ω (see the purple curve in Fig. 10(a)-(b)). The rapid periodic change in ω is, instead, due to the activation/deactivation of the $C_2^{(b)}$ compartment. Under cyclic conditions, the rate of DNA synthesis falls below v_+ but remains well above its minimum value $v_- \approx 5 \times 10^{-3}$. Despite the marked fluctuations in the velocity v, τ_S increases almost steadily (albeit at a lower rate than for E_1) until it plateaus at a maximum value of ≈ 22 hours.

As shown in Fig. 11, constant and cyclic RH also affect the evolution of the distribution $s(x, t)$. Under constant RH (E_1, see pink curves), cells tend to accumulate near $x \approx 1$. Due to the low rate of DNA synthesis, the profile appears approximately stationary. In particular, comparison of the pink curves in panels (b) and (c) suggests that the discontinuity in the profile has barely moved. While for scenario E_1, $s(x, t)$ is characterised by a single slow-moving front, for scenario E_2 (see purple curves) the front is followed by a series of asymmetric spikes which propagate along the x-axis with velocity v (see Fig. 9(e)). Each spike corresponds to cells in the C_1 compartment quickly re-entering the cell-cycle transitioning S phase after re-oxygenation; these cells remain highly synchronised as they proceed through the S phase. Since there is no re-oxygenation in E_1, spikes are not observed. Focusing on the purple curve in Fig. 11(c), and moving from left ($x = 1$) to right ($x = 2$), the peak value decreases (as the spikes become wider). However, at later times (see Fig. 11(e)), the left-most spikes have lower peaks due to the depletion of cells in the P_1 population (see Fig. 9).

Overall, our results suggest that, while both constant and cyclic RH lead to a slow down of proliferation, they do so via distinct biological mechanisms. In the first case, cells arrest in the C_1 compartment and DNA synthesis is almost completely inhibited. On the other hand, under cyclic hypoxia (E_2), DNA synthesis proceeds, albeit at a lower rate. This leads to an increase in τ_S and cell accumulation in the S phase. Despite being able to complete the S phase, cells later arrest in the $C_2^{(a)}$ checkpoint. This, however, is evident only at long times (≈ 24 hr), when we see a large accumulation of diploid cells. Our findings are in line with the experimental data in Fig. 2 (which are taken from Bader et al., 2021), indicating that our model can capture the experimentally observed cell-cycle dynamics.

Next, we use our model to investigate modes of cyclic RH not yet tested in the laboratory. For example, in Fig. 12, we fix the length of the RH phase to 2 hr and compare the growth curves for different durations of reoxygenation. We find that when the reoxygenation periods are significantly longer than the time cells spend in RH, cells have time to recover and continue proliferating,

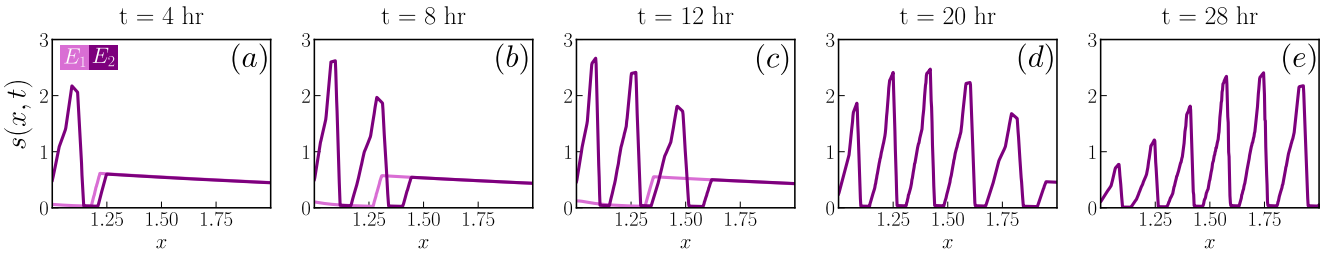

Fig. 11. Evolution of the DNA distribution, $s(x,t)$, computed by numerically solving Eq. (9) for the two cases in Fig. 9: acute RH (pink curve-E_1) and cyclic RH (purple curve-E_2). The parameters are chosen as in Fig. 9.

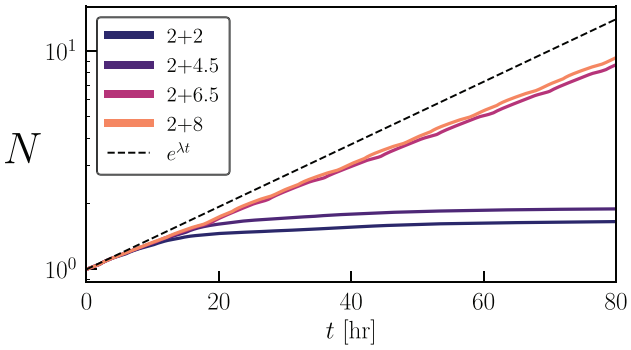

Fig. 12. Evolution of the total cell number $N(t)$ for different oxygen cycles as predicted by Eqs. (17). While the time spent in RH is constant for all experiments (i.e., 2 hr), we change the length of the reoxygenation phase (from 2 hr as in Fig. 9(b) to 8 hr). We also include, as a control case, the PSS (black dashed line). Parameters are chosen as in Fig. 9.

albeit at a lower rate. As shown in Fig. 13, even when cyclic RH does not significantly reduce proliferation (i.e., cycles 2 + 6.5 and 2 + 8 in Fig. 12), it can still affect the cell-cycle distribution when compared to the predictions for the phase stationary solution (represented by the dashed line). For the example in Fig. 13(a), cyclic RH eventually leads to $f_s(t)$ being above its initial value $\bar{f}_s$. This is relevant when thinking about cell-cycle specific treatment. Since cyclic RH changes the distribution of cells along the cycle, it can impair or favour treatment efficacy. For example, we know that cells in different phases of the cell-cycle have different responses to radiotherapy (Pawlik and Keyomarsi, 2004). In this case, cells in the G2/M phase have been shown to be the most sensitive to radiotherapy (Pawlik and Keyomarsi, 2004). Referring to Fig. 13 (a), we note that persistent exposure to cyclic hypoxia biases the cell-cycle distribution to the S phase. As such, it could decrease the overall sensitivity of cells to RT, even during reoxygenation, when oxygen levels do not directly increase cell radio-resistance. When considering longer re-oxygenation periods, such as in Fig. 13(b), we observe larger fluctuations in the cell fractions. Towards the end of the re-oxygenation phase, f_2 is just above the value $\bar{f}_2$. This suggests that applying treatment at this time could improve treatment efficacy. However, if treatment is not timed accurately and is applied when f_2 is at its minimum, or when cells are in RH, then cyclic hypoxia could, instead, favour radio-resistance. This highlights the possible use of mathematical models to predict cell-cycle dynamics and how this can affect treatment outcomes when testing protocols *in vitro* accounting also for other mechanisms (such as oxygen) that can affect treatment outcomes. In order to achieve this, robust calibration of the model to experimental data is needed.

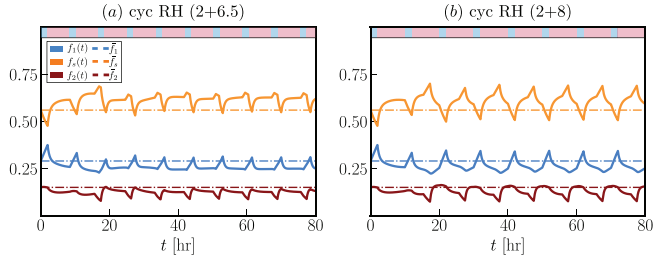

Fig. 13. Evolution of the cell fraction f_m (see solid lines) with $m \in \{1,s,2\}$ as predicted by the model for two different cyclic protocols in Fig. 12: (a) 2 hr ($< 0.2\%$) + 6.5 hr (2%) or (b) 2 hr ($< 0.2\%$) + 8 hr (2%). We compare the dynamics in cyclic RH with the PSS ($\bar{f}_m$) indicated by the dotted line. The parameters are chosen as in Fig. 9.

5.2. A class of models: comparison of different modelling assumptions

The model defined by Eqs. (17) is complex in its response to variable oxygen levels. While we have shown that the model agrees qualitatively with the experimental data, it is unclear whether all four mechanisms introduced in §2 are necessary to explain the experimental observations. To answer this question, we construct a class of models, $\mathbb{M}$, obtained by systematically reducing the complexity of the full model. A list of the models considered is presented in Table 3. While all models reduce to Eqs. (19) under normoxia, they differ in their response to RH. The alternative models are derived from the full model, named $\mathscr{M}_0$, by fixing either $C_1 \equiv 0$ ($\mathscr{M}_1$), $C_2^{(a)} \equiv 0$ ($\mathscr{M}_2$) or/and $C_2^{(b)} \equiv 0$ ($\mathscr{M}_3$ and $\mathscr{M}_4$). Here models $\mathscr{M}_1$ to $\mathscr{M}_4$ test which of the checkpoint compartments are needed to describe the experimental data. The last two rows of Table 3 list the unknown model parameters associated with each model; while all models share the parameters $\boldsymbol{\theta}$, they vary in the number of parameters $\boldsymbol{\Theta}$ associated with RH. In particular, the number of unknown parameters associated with model $\mathscr{M}_k$ decreases as k increases (i.e., as the model complexity reduces). As we will detail in §6, we calibrate all models to the data in Fig. 2, and in Fig. 14 and Fig. 15, we compare the resulting fits. In doing so we consider the predictions from the full model $\mathscr{M}_0$ (see white dotted line in the plots) as representative of the experimental observations.

In Fig. 14, we compare model predictions when cells are exposed to constant RH (E_1). In this case all models, except $\mathscr{M}_1$, predict that f_1 increases in line with the experimental observations from Bader et al. (2021). In contrast, model $\mathscr{M}_1$ (Fig. 14(c)) is incompatible with the experimental data, predicting a monotonic decrease in $f_1(t)$ and cell accumulation in S phase (observe the large increase in $f_s(t)$ over time). This suggests that under constant RH, the C_1 checkpoint plays a key role. By contrast, since the simpler model $\mathscr{M}_4$ predicts the same trends as those observed for model $\mathscr{M}_0$, we deduce that both C_2 checkpoints (i.e., $C_2^{(a)}$ and $C_2^{(b)}$) can be neglected. Moving on to Fig. 15, we find that neglecting the C_1 checkpoint does not significantly impact predictions under cyclic RH. Indeed, Fig. 15(a) shows that model $\mathscr{M}_1$ is in qualitative

Table 3
Schematics showing the biological mechanisms (see §2 for the explanation of the mechanisms (1)-(4)) included in each model $\mathscr{M}$ belonging to the class of models $\mathbb{M}$. We also indicate the list of unknown parameter sets $\boldsymbol{\theta}$ and $\boldsymbol{\Theta}$ associated with each model $\mathscr{M}_k$ where the first set determines the phase stationary solution, while the second set plays a role in the oxygen dependent mechanisms (Mech 1)-(Mech 4). The full model, $\mathscr{M}_0$, has the largest number of parameters (i.e. higher complexity) but it accounts for all the mechanisms we expect to play a role in cell-cycle dynamics under cyclic hypoxia.

	$\mathscr{M}_0$	$\mathscr{M}_1$	$\mathscr{M}_2$	$\mathscr{M}_3$	$\mathscr{M}_4$
	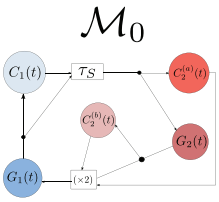	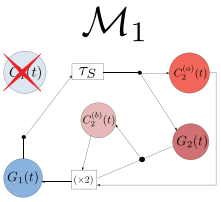	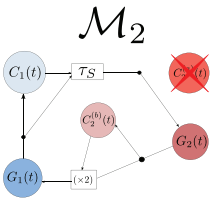	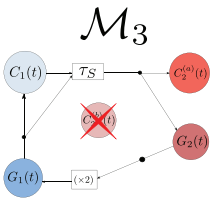	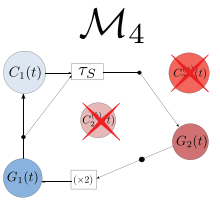
Mech 1	True	True	True	True	True
Mech 2	True	False ($C_1 \equiv 0$)	True	True	True
Mech 3	True	True	False ($C_2^{(a)} \equiv 0$)	True ($\alpha_2 = 0$)	False($C_2^{(a)} \equiv 0$)
Mech 4	True	True	True	False ($C_2^{(b)} \equiv 0$)	False($C_2^{(b)} \equiv 0$)
$\boldsymbol{\theta}$	$[k_1, v_+, k_2]$	$[k_1, v_+, k_2]$	$[k_1, v_+, k_2]$	$[k_1, v_+, k_2]$	$[k_1, v_+, k_2]$
$\boldsymbol{\Theta}$	$[K_1, q_1, \mathscr{R}_+, \mathscr{R}_-, p, T, \alpha_2, q_2, K_2]$	$[\mathscr{R}_+, \mathscr{R}_-, p, T, \alpha_2, q_2, K_2]$	$[K_1, q_1, \mathscr{R}_+, \mathscr{R}_-, q_2, K_2]$	$[K_1, q_1, \mathscr{R}_+, \mathscr{R}_-, p, T]$	$[K_1, q_1, \mathscr{R}_+, \mathscr{R}_-]$

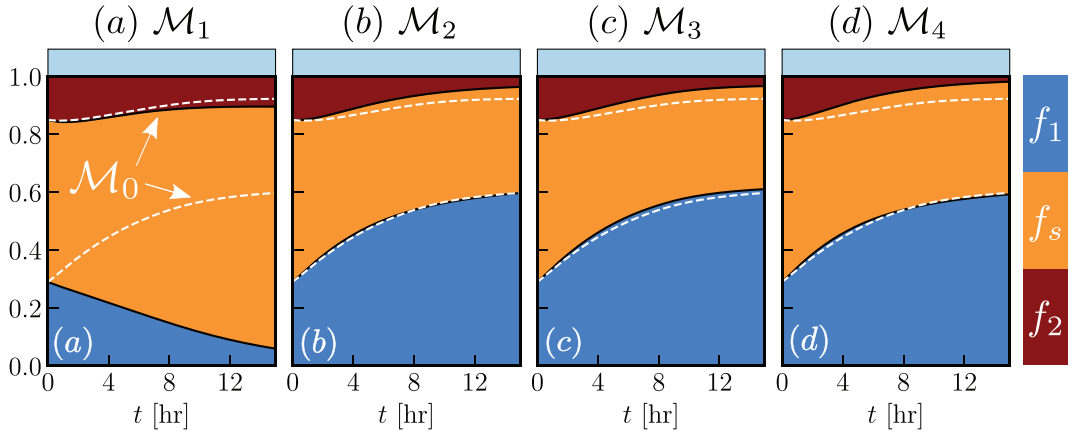

Fig. 14. Comparison of the cell-cycle dynamics predicted by solving numerically the models $\mathscr{M}_1$-$\mathscr{M}_4$ listed in Table 3 for constant RH (scenario E_1). We here use the best fit obtained for each model. The white dotted lines in the panels indicate the evolution predicted by model $\mathscr{M}_0$, used here as a reference. The parameters k_1, $v_\pm$ and k_2 are as in Table 2, while the oxygen-dependent parameters $\boldsymbol{\Theta}$ are taken to be the estimated mean values reported in Table C.9.

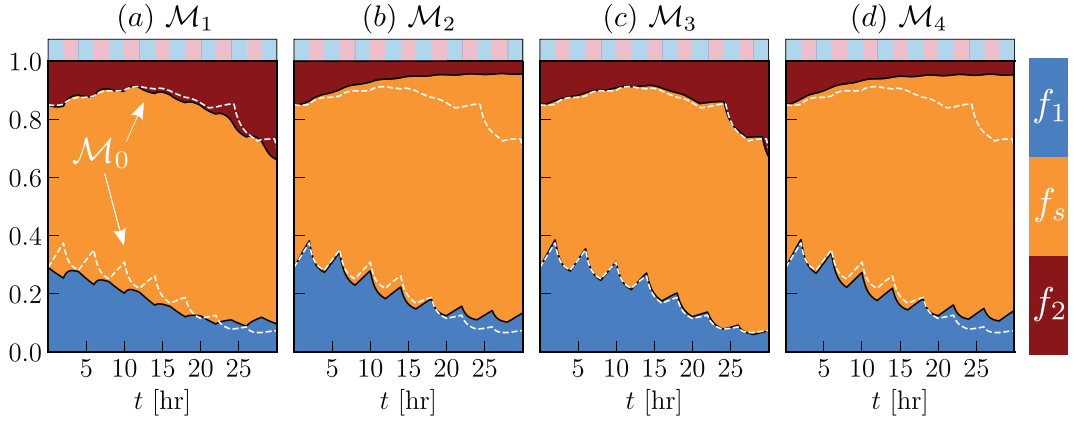

Fig. 15. Comparison of the cell-cycle dynamics predicted by solving numerically the models $\mathscr{M}_1$-$\mathscr{M}_4$ listed in Table 3 for cyclic RH (scenario E_2). We here use the characteristic fits obtained for each model (see Table in C). The white dotted lines in the panels indicate the evolution predicted by model $\mathscr{M}_0$, used here as a reference. The parameters k_1, $v_\pm$ and k_2 are as in Table 2, while the oxygen-dependent parameters $\boldsymbol{\Theta}$ are taken to be the estimated mean values reported in Table C.9.

agreement with model $\mathscr{M}_0$. While $\mathscr{M}_1$ does not capture the rapid fluctuations in $f_1(t)$ predicted by $\mathscr{M}_0$, the overall trend is the same, with $f_1(t)$ decreasing after each cycle. Focusing on Figs. 15(b) and 15(d), we see good agreement with $\mathscr{M}_0$ until $t \approx 10$ hr. At later times, both models $\mathscr{M}_2$ and $\mathscr{M}_4$ underestimate the values of f_2 and fail to capture the late accumulation of cells in the G2/M phase observed experimentally (see Fig. 2). Interestingly, the predictions of model $\mathscr{M}_2$ are similar to those of model $\mathscr{M}_4$ (where both C_2 checkpoints are neglected). This is because, when the model is fitted to the data, the probability q_2 of cells arresting in $C_2^{(b)}$ is esti-

mated to be small, taking the value $q_2 = 0.08$. This suggests that including mitotic arrest due to lack of oxygen via the $C_2^{(b)}$ checkpoint does not help to explain the experimental observations. Given that model $\mathscr{M}_3$ matches the expected behaviour, we conclude that the $C_2^{(a)}$ checkpoint is needed for the model to explain the cell-cycle dynamics observed under cyclic RH conditions. This suggests that memory effects are more likely to be driving cell arrest under cyclic RH than instantaneous sensing of low oxygen levels. On the contrary, memory effects can be neglected under conditions of acute chronic RH.

From the results in Figs. 14 and 15 it is apparent that the models $\mathscr{M}_1, \mathscr{M}_2$ and $\mathscr{M}_4$ are unable to recapitulate experimental observations. In contrast, the predictions from $\mathscr{M}_0$ and, the far simpler model, $\mathscr{M}_3$ are both in agreement with the experimental data. Choosing which model between $\mathscr{M}_0$ and $\mathscr{M}_3$ is best supported by experimental observation is, therefore, not straightforward and requires consideration of other metrics, in addition to how well they fit the experimental data. These questions will be addressed in the next section, where we implement Bayesian model selection.

6. Parameter fitting and model selection

So far, we have presented model predictions for point estimates of the model parameter values. In this section, we explain how such estimates were obtained and investigate how the results in §5 change when we account for uncertainty in the estimates of "oxygen-dependent" parameters. We start by using the data from the balanced exponential growth experiments (E_0) to determine the "oxygen-independent" parameters $\boldsymbol{\theta}$ using the results from §4. As mentioned in §5.2, all models $\mathscr{M} \in \mathbb{M}$ reduce to the same set of equations (Eqs. (19)) in normoxia. As such, they share the same value $\boldsymbol{\theta}$. We then focus on estimating the remaining parameters $\boldsymbol{\Theta}$, which determine the system response to dynamic oxygen conditions. Here we will compare different modelling assumptions by applying model selection methods. We start by fitting each model $\mathscr{M}_k$ in Table 3 to experimental data from both constant (E_1) and cyclic (E_2) RH simultaneously, using Bayesian inference and Monte Carlo methods to estimate the posterior distribution, π_{ps}, for the parameters $\boldsymbol{\Theta}$ (more details follow). We then select the "best" candidate model by using the deviance information criterion (DIC) as an estimate of model performance, and briefly discuss parameter identifiability based on posterior profiles.

6.1. Estimation of oxygen independent parameters

We recall from §4, that the regime of unperturbed exponential growth is characterised by the value of the constants $(\bar{f}_1, \bar{f}_2, \lambda)$. As explained further in Appendix A, these constants uniquely define the values of the parameters (k_1, k_2, ν_+) as given by Eqs. (A.7). In practice, we can estimate the stationary values $\bar{f}_1$ and $\bar{f}_2$ using flow cytometry data. However, additional data are needed to determine the proliferation rate λ. This parameter can be related to the population doubling time, T_{doub} (Basse et al., 2003), which is known for most cell lines when cultured in standard media and in the absence of competition (i.e., low confluence). It is straightforward to show that $T_{doub} = \lambda^{-1} \ln 2$.

Given that, prior to any of the experiments in Bader et al. (2021), the cells were cultured at 21% O_2, with re-plating in order to minimise any effects due to contact inhibition, we assume that initially the cells are undergoing exponential growth. We can, therefore, use the cell fractions data reported at time $t = 0$ in Fig. 2 to estimate the values of $\bar{f}_1$ and $\bar{f}_2$. For simplicity, we suppose that median values provide a good approximation to the 'true' cell fractions so that $\bar{f}_1 \sim 0.29$ and $\bar{f}_2 \sim 0.15$. In this way, we can obtain point estimates for $\vec{\boldsymbol{\theta}}$ which facilitates the identification of the remaining model parameters $\vec{\boldsymbol{\Theta}}$. In previous experiments, the doubling time of RKO cells has been estimated to be about 21 hr (Witzel et al., 2015). The corresponding parameter estimates (obtained using Eq. (A.7)) are listed in Table 4 together with estimates of the duration of each cell cycle phase (given by the inverse of the rates of k_1, k_2 and ν_+ (Basse et al., 2003)). We note that the RKO cell line is characterised by a particularly long S phase with cells spending, on average, as much time in S phase as in the G1 and G2/M phases combined.

6.2. Calibration of the candidate models to time-series flow-cytometry data

The second step concerns estimation of the parameters $\boldsymbol{\Theta}$ which are associated with the oxygen-dependent mechanisms. Here we use Bayesian inference (Lambert, 2018), which allows us to account for measurement errors and to assess uncertainty in the parameter estimates.

Given the small amount of data available, we calibrate the model by pooling all the data available from both the constant RH (E_1) and the cyclic RH (E_2) experiments. We therefore postpone model validation until more data will be available. In Fig. 2, for each time point, we reported the mean and standard deviation over multiple runs of the experiments; however, for the estimation of $\boldsymbol{\Theta}$ we consider individual experimental measurements, instead of summary statistics. The complete data set can be found in Appendix B. We denote by $F_m^{(i,j)}$ the i-th measurement of the fraction of cells in the subpopulation F_m ($m \in \{1, s, 2\}$ performed at time $t^{(i,j)}$ during experiment E_j with $j \in \{1, 2\}$. Given that F_1, F_s and F_2 are not independent (recall $F_s = 1 - F_1 - F_2$), we only consider observations for F_1 and F_2 in the fitting. We collect the data in the set $\mathscr{E} = \left\{\left(t^{(i,1)}, {F_1}^{(i,1)}, {F_2}^{(i,1)}\right)\right\}_{i=1}^{L_1} \cup \left\{\left(t^{(i,2)}, {F_1}^{(i,2)}, {F_2}^{(i,2)}\right)\right\}_{i=1}^{L_2}$, where $L_1 = 4$ and $L_2 = 14$ are the number of measurements collected in experiments E_1 and E_2, respectively.

The observation model. Let us now denote by $f_m(t; \boldsymbol{\Theta}, \mathscr{M}, E_j)$ (with $m \in \{1, 2\}$) the value of the cell fractions at time t for the experimental scenario E_j predicted by the model $\mathscr{M} \in \mathbb{M}$ for parameter values $\boldsymbol{\Theta}$. We here consider the experimental observations $F_m^{(i,j)}$ to be noisy realisations of the model solutions, $f_m(t^{(i,j)}; \boldsymbol{\Theta}, \mathscr{M}, E_j)$. We assume that the observation errors are independent, additive and normally distributed with zero mean and variance σ_m^2. Furthermore, we consider σ_m to be constant in time and to be the same for both constant (E_1) and cyclic (E_2) experiments. Instead of specifying the values of the variance σ_1 and σ_2, we treat them as unknown parameters that are learnt from the

Table 4
Estimates of the cell-cycle parameters for the RKO cell line obtained using the phase stationary solution (PSS) and the experimental data from Bader et al. (2021).

	Transition rates [hr^{-1}]	Average time in the compartment [hr]	Cell fractions (from Bader et al., 2021)
G1	$k_1 = 0.195$	$\tau_1 \approx k_1^{-1} \approx 5.14$	$\bar{f}_1 = 0.29$
S	$\nu_+ = 0.083$	$\tau_S = \nu_+^{-1} \approx 12$	$\bar{f}_s = 0.56$
G2/M	$k_2 = 0.22$	$\tau_2 \approx k_2^{-1} \approx 4.54$	$\bar{f}_2 = 0.15$

data. Since the cell fractions are normalised, we assume that σ_1 and σ_2 are uniformly distributed in $[0,1]$ (*i.e.*, $\pi(\boldsymbol{\sigma}) \sim U(0,1) \times U(0,1)$).

The likelihood function $\mathscr{L}_{\mathscr{M}}(\mathscr{E}|\boldsymbol{\Theta})$ represents the probability of observing the experimental data $\mathscr{E}$ under the model $\mathscr{M}$ with parameter values $\boldsymbol{\Theta}$. Based on the assumptions outlined above, $\mathscr{L}_{\mathscr{M}}$ reads:

$$\mathscr{L}_{\mathscr{M}}(\mathscr{E}|\boldsymbol{\Theta},\boldsymbol{\sigma}) = \prod_{m=1}^{2}\prod_{j=1}^{2}\prod_{i=1}^{L_j}\phi\left(F_m^{(i,j)}; f_m\left(t^{(i,j)};\boldsymbol{\Theta},\mathscr{M},E_j\right),\sigma_m^2\right), \tag{23}$$

where $\boldsymbol{\sigma} = [\sigma_1,\sigma_2]$, and ϕ is the normal probability density with mean $f_m(t;\boldsymbol{\Theta},\mathscr{M},E_j)$ and variance σ_m^2.

Calibration and model selection. Given the model $\mathscr{M}$ from the class $\mathbb{M}$, any prior information on its parameter values is captured by the prior distribution, $p_{\mathscr{M}}(\boldsymbol{\Theta})$. In the absence of prior information about the values of the model parameters $\boldsymbol{\Theta}$, we assume that each model parameter (i.e., Θ_i for $i = 1,\dots,\kappa(\mathscr{M})$), is uniformly distributed on the intervals $[\underline{\Theta}_i,\bar{\Theta}_i]$, where the extremes of the intervals are taken from Table 2; hence $\pi_{\mathscr{M}}(\boldsymbol{\Theta})$ is given by:

$$\pi_{\mathscr{M}}(\boldsymbol{\Theta}) = \prod_{i=1}^{\kappa(\mathscr{M})}\left(\bar{\Theta}_i - \underline{\Theta}_i\right)^{-1}\mathbb{1}_{\Omega_{\mathscr{M}}}(\boldsymbol{\Theta}), \tag{24}$$

where $\mathbb{1}_{\Omega_{\mathscr{M}}}$ is the indicator function for the support of the uniform distribution, i.e., $\Omega_{\mathscr{M}} = [\underline{\Theta}_1,\bar{\Theta}_1] \times \dots \times [\underline{\Theta}_{\kappa(\mathscr{M})},\bar{\Theta}_{\kappa(\mathscr{M})}]$.

Using Bayes' Theorem, we can update our prior distributions $(\pi_{\mathscr{M}}(\boldsymbol{\Theta}),\pi(\boldsymbol{\sigma}))$ in light of the experimental data available:

$$\pi_{\mathscr{M}}(\boldsymbol{\Theta},\boldsymbol{\sigma}|\mathscr{E}) = \frac{\pi_{\mathscr{M}}(\boldsymbol{\Theta})\pi(\boldsymbol{\sigma})\mathscr{L}_{\mathscr{M}}(\mathscr{E}|\boldsymbol{\Theta},\boldsymbol{\sigma})}{p(\mathscr{E})}, \tag{25a}$$

where $p(\mathscr{E})$ is a normalising factor and $\pi_{\mathscr{M}}(\boldsymbol{\Theta},\boldsymbol{\sigma}|\mathscr{E})$ is the posterior distribution for model $\mathscr{M}$.

Due to the dimensions of our parameter space, it is not possible to compute Eq. (25a) analytically. Instead we rely on Markov Chain Monte Carlo (MCMC) methods to estimate $\pi_{\mathscr{M}}(\boldsymbol{\Theta},\boldsymbol{\sigma}|\mathscr{E})$ using the python package PINTS (Probabilistic Inference on Noisy Time-Series) for Bayesian inference (Clerx et al., 2019). More details on the numerical technique are included in Appendix C.

For model selection among the class of models $\mathbb{M}$, we compute the deviance information criterion (DIC) (Gelman et al., 2013; Lambert, 2018). The DIC represents a trade-off between model complexity (as measured by the over-fitting bias k_{DIC}) and model accuracy (as measured by the likelihood). Given a model $\mathscr{M}$, the DIC is defined as follows (Lambert, 2018):

$$\mathrm{DIC}(\mathscr{M}) = 2k_{DIC}(\mathscr{M}) - 2\ln\left(\hat{\mathscr{L}}_{\mathscr{M}}\right), \tag{26a}$$

$$\text{with } k_{DIC}(\mathscr{M}) = 2\mathrm{Var}[\ln \mathscr{L}_{\mathscr{M}}|\mathscr{E}], \tag{26b}$$

where $\hat{\mathscr{L}}_{\mathscr{M}} = \mathscr{L}_{\mathscr{M}}\left(\mathscr{E}|\hat{\boldsymbol{\Theta}},\hat{\boldsymbol{\sigma}}\right)$ is the likelihood value estimated at the expected value of the unknown parameters (*i.e.,* $\hat{\boldsymbol{\Theta}}$ and $\hat{\boldsymbol{\sigma}}$) whose components are given by

$$\hat{\Theta}_i = \int_{[0,1]^2}\int_{\Omega_{\mathscr{M}}} \Theta_i\,\pi_{\mathscr{M}}(\boldsymbol{\Theta},\boldsymbol{\sigma}|\mathscr{E})d\boldsymbol{\Theta}d\boldsymbol{\sigma}, \quad i = 1,\dots\kappa(\mathscr{M}), \tag{26c}$$

$$\hat{\sigma}_i = \int_{[0,1]^2}\int_{\Omega_{\mathscr{M}}} \sigma_i\,\pi_{\mathscr{M}}(\boldsymbol{\Theta},\boldsymbol{\sigma}|\mathscr{E})d\boldsymbol{\Theta}d\boldsymbol{\sigma}, \quad i = 1,2. \tag{26d}$$

In Eq. (26b) Var is the variance of the log-likelihood, $\ln \mathscr{L}_{\mathscr{M}}$, here approximated via sampling from the estimated posterior. When comparing models, we are interested in the relative value of the DIC, and favour the model with the smaller DIC. We note that the DIC penalises models with large values of k_{DIC}, to account for the fact that complex models are more likely to fit data well. More complex models tend to have more parameters which can lead to higher posterior uncertainty if the model is too complex for the data (i.e., it is over-fitted) (Lambert, 2018). This results in a larger variability in the expected log-likelihood (i.e., larger k_{DIC}). In other words, the term k_{DIC} in Eq. (26a) corrects for over-fitting.

For a model $\mathscr{M}$, predictive posterior estimates are obtained by sampling 800 parameter sets, $\left(\boldsymbol{\Theta}^{(i)},\boldsymbol{\sigma}^{(i)}\right)$, from the estimated posterior $\pi_{\mathscr{M}}(\boldsymbol{\Theta},\boldsymbol{\sigma}|\mathscr{E})$. For each set, we run the model $\mathscr{M}$ forwards to generate 800 predictive curves for each fraction $f_m^{(i)}(t)$ with $m \in \{1,2\}$ and $i = 1,\dots,800$. This gives posterior distributions for the *"true"* cell fraction. To obtain posterior distributions for the *measured* cell fractions $F_m^{(i)}(t)$, we add to the simulated cell fractions $f_m^{(i)}(t)$ the corresponding measurement errors $e_m(t) \sim \mathscr{N}\left(0,\sigma_m^2\right)$. We then estimate $F_s^{(i)}$ as $F_s^{(i)} = 1 - F_1^{(i)} - F_2^{(i)}$ and $f_s^{(i)}$ as $f_s^{(i)} = 1 - f_1^{(i)} - f_2^{(i)}$. At each time point, we compute the mean of the 800 predictive curves (for either the "true" or measured fractions) and the corresponding 68%- and 95%-confidence intervals. For the plots in §5, we used the expected values $\hat{\boldsymbol{\Theta}}$ (see Eqs. (26c)) as representative of characteristic model fits. Additional results on the estimated posterior distributions can be found in Appendix C.

6.2.1. Numerical results

The estimated DICs for the models $\mathscr{M} \in \mathbb{M}$ are reported in Table 5. Based on these estimates, model $\mathscr{M}_0$ has the lowest DIC and is, therefore, the "best" model in the class $\mathbb{M}$. As expected from the results presented in §5.2, $\mathscr{M}_1$, $\mathscr{M}_2$ and $\mathscr{M}_4$ all exhibit poor performance. In this case, the difference in the estimated DICs is rooted in the value of $\hat{\mathscr{L}}_{\mathscr{M}}$, which is markedly reduced suggesting that these three models fail to fit the experimental data. We conclude that including the C_1 and $C_2^{(a)}$ compartments (*i.e.* cell-cycle arrest in the G1 and G2 phases) is necessary for our model to reproduce the experimentally observed cell-cycle dynamics. On the contrary, adding the $C_2^{(b)}$ compartment does not seem to play a relevant role in explaining the experimental data.

We see that model $\mathscr{M}_3$, which neglects the compartment $C_2^{(b)}$, is only slightly worse then $\mathscr{M}_0$. The two models yield similar values of $\hat{\mathscr{L}}_{\mathscr{M}}$ and similar estimated values of k_{DIC}. This suggests that the additional complexity due to the introduction of the $C_2^{(b)}$ compartment plays only a minor role in explaining the cell-cycle dynamics reported experimentally. While we will employ model $\mathscr{M}_0$ in the remainder of the paper, additional experiments and data are needed to determine whether arrest of cells in G2/M due to low oxygen levels (as captured by the compartment $C_2^{(b)}$) is biologically relevant or might be an artefact of measurement errors and the small number of data points currently available. This interpretation is confirmed by the profile of the marginal posterior for q_2 (see Fig. 18), whose mean value is approximately $q_2 = 0.16$, indicating a very small probability of cells arresting in $C_2^{(b)}$. This is in contrast to the value of q_1, for which the posterior distribution peaks at $q_1 \approx 1$. We conclude that the instantaneous response of cells to low oxygen levels is to arrest in the G1 phase while they still proceed to mitosis.

Candidate model $\mathscr{M}_0$ is in good agreement with the experimental data. Our analysis shows that model $\mathscr{M}_0$ gives the best fit to the experimental data. Referring to the posterior predictions in Fig. 16, we note that $\mathscr{M}_0$ captures the experimental data from both experiments E_1 and E_2, with all experimental data points falling within the 95%-confidence interval of the posterior predictions for the "measured" fractions, F_1, F_s and F_2.

Interestingly, the model predicts that α_2, the rate at which cells exit the $C_2^{(a)}$ compartment, is small, with the posterior distribution on this parameter (see Fig. 18(g)) being narrowly skewed towards $\alpha_2 = 0$. This is in line with our expectation since the RKO cancer cell line under consideration is known to be p53-competent. This

Table 5
Comparison based on the deviation information criterion (DIC) of the models in class $\mathbb{M}$ that were introduced in §5.2. The last column indicates the relative *DIC* score with respect to model $\mathscr{M}_0$, i.e., ΔDIC = DIC($\mathscr{M}$)-DIC($\mathscr{M}_0$).

	k_{DIC}	$\ln(\hat{\mathscr{L}}_{\mathscr{M}})$	DIC	ΔDIC
$\mathscr{M}_0$	5.87	67.98	−124.22	0
$\mathscr{M}_1$	6.31	41.82	−71.01	49.21
$\mathscr{M}_2$	4.74	46.14	−82.79	37.43
$\mathscr{M}_3$	5.85	65.99	−120.27	3.95
$\mathscr{M}_4$	4.25	45.84	−83.18	37.04

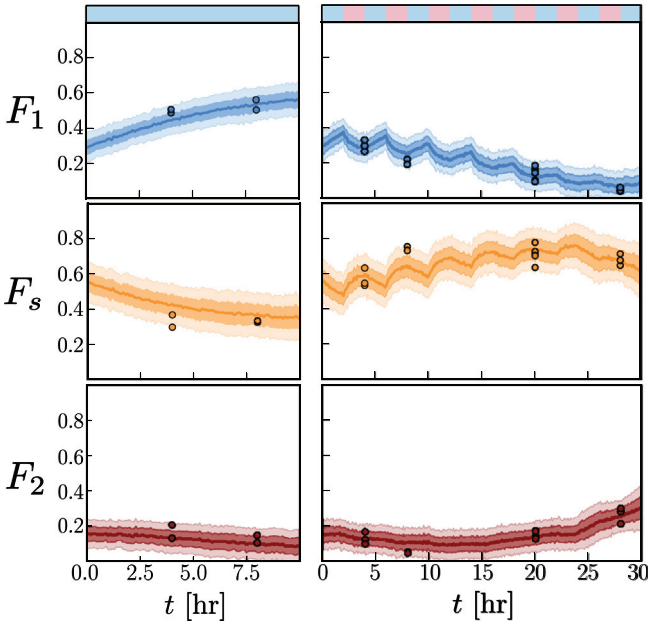

Fig. 16. Posterior prediction distribution of the selected model $\mathscr{M}_0$ for (left) chronic RH and (right) cyclic RH. For both scenarios we plot the predicted measured fractions $F_m(t)$ with $m \in \{1, s, 2\}$ and compare them with the experimental data (dots). For each model output, we plot the expected values, together with the 68%- and 95%-confidence intervals, as indicated by the dark and light shaded areas, respectively.

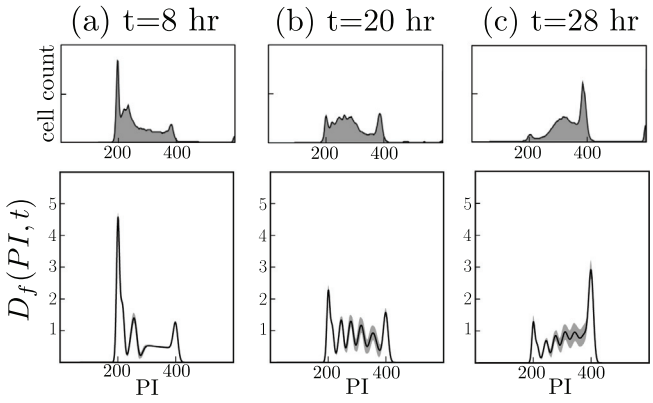

Fig. 17. Posterior prediction for the distribution D_f as defined by Eq. (26a) for cyclic RH (E_2). The dark line indicates the average over 800 parameter sets sampled from the estimated posterior, while the shaded grey area indicates the 68% confidence interval. At each time point, we compare the theoretical prediction (bottom panels) with the experimentally measured distribution from Fig. 3 in Bader et al. (2021) (top panels). Fluorescence readings of PI = 200 and PI = 400 correspond, respectively, to $x \approx 1$ and $x \approx 2$. This comparison is qualitative, as the vertical axes for the theoretical (bottom panels) and experimental (top panels) distributions are different since D_f is re-scaled by the number of cells $N(t)$, while the experimental output is in terms of absolute cell counts.

may not be true for other cell lines, particularly if they are p53-deficient, given the role of p53 in mediating G2 arrest in several cancer cells (Taylor and Stark, 2001).

Fig. 17 shows that $\mathscr{M}_0$ can also capture the qualitative shape of the flow cytometric distribution (D_f) reported in Bader et al. (2021), which indicates cell number as a function of PI-fluorescence intensity (see Fig. 1). We note that while the experimental observations relate to only one realisation, we illustrate the expected profile over several model realisations. Here we estimate D_f using output from the numerical solution of Eqs. (17) as follows: based on Basse et al., (2005), we assume that a population of cells with the same DNA content x gives rise to a Gaussian-like flow cytometric output (see Fig. 1); consequently, we model the flow cytometric output D_f as

$$D_f(\mathrm{PI}, t) = \int_1^2 h(\mathrm{PI}|x)\mathscr{D}(x,t)dx, \tag{26a}$$

where

$$\mathscr{D}(x,t) = f_1(t)\,\delta(x-1) + s(x,t) + f_2(t)\,\delta(x-2), \tag{26b}$$

and $\delta(x-y)$ is the delta function, (*i.e.*, $\delta = 1$ if $x = y$ and $\delta = 0$ otherwise). The term $h(\mathrm{PI}|x)$ in Eq. (26a) is the probability of recording a fluorescence intensity PI for a cell with DNA content x and has the form

$$h(\mathrm{PI}|x) = \frac{1}{\sqrt{2\pi}\alpha\gamma(x)} \exp\left[-\frac{(\mathrm{PI}-\alpha x)^2}{2\alpha^2\gamma(x)^2}\right]. \tag{26c}$$

In Eq. (26c), we assume that the mean PI fluorescence is proportional to the DNA content x, with constant of proportionality $\alpha = 200$ PI, so that $x = 1$ corresponds to a fluorescence intensity PI = 200. Following Basse et al., (2005) again, we suppose that the variance γ depends linearly on x (*i.e.*, $\gamma = (\gamma_2 - \gamma_1)(x-1) + \gamma_1$, with $\gamma_{1,2}$ being the variances associated with DNA contents of $x = 1$ and $x = 2$, respectively). In general, γ_1 and γ_2 will depend on the cell line of interest. Since here we are interested in qualitative comparisons, we set $\gamma_1 = 0.025$ and $\gamma_2 = 0.04$, which gives good agreement with the G1 and G2/M peak width.

Given that the calibration only uses information about cell fractions, the agreement between our theoretical estimates for D_f and the experimental observations is encouraging (see Fig. 17). However, there are some non-negligible discrepancies, particularly at time $t = 20$ hr. The model predicts a higher percentage of cells in late S phase, so that the peak corresponding to PI = 400 is not isolated; in contrast the experimental profile tends to flatten in the vicinity of PI ≈ 350, so that the peak at PI ≈ 400 is isolated. The discrepancies between model predictions and experimentally observed DNA profiles suggest that aspects of the biology that can affect the full flow cytometry profile might be missing from

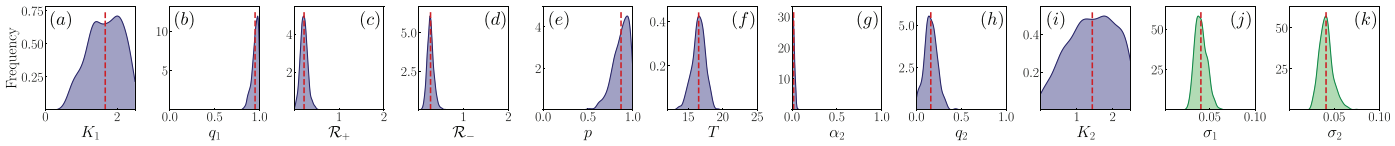

Fig. 18. Marginal posterior distributions $\pi_{\mathscr{M}_0}(\Theta|\mathscr{E})$ for the model parameters $\Theta \in \{K_1, q_1, \mathscr{R}_+, \mathscr{R}_-, p, T, \alpha_2, q_2, K_2\}$ and the error parameters $\pi_{\mathscr{M}_0}(\sigma_i|\mathscr{E})$ for $i = 1, 2$. The red vertical line indicates the mean value as reported in Table C.9. We see that for most parameters the posterior distribution has a narrow support. This is not the case for K_1 *and* K_2 (see panels (a) and (i)) where the broader support of the posterior is a sign of practical non-identifiability.

the model. For example, our model neglects variability in the DNA synthesis velocity which, while not significantly affecting summary statistics such as cell fractions, could have a significant impact on the profile of the flow cytometry output D_f. This feature could be added into the model by using a similar framework to the one proposed by Basse et al. (2003). Alternatively, the DNA profile observed experimentally might be explained by assuming that the transition of cells in and out of the C_1 compartment might be delayed in response to changes in oxygen levels. This would suggest that cells maintain some sort of inertia and would further question the standard assumption in the literature that cells respond instantaneously to oxygen levels. Further analysis is needed to determine which (if any) of the proposed explanations accounts for the observed discrepancy. Since we are interested in capturing the overall cell-cycle dynamics, we postpone such investigations to future work.

Model Identifiability. We end our discussion on model calibration by briefly considering practical identifiability of the unknown parameters. Following Daly et al., (2018) and Hines et al., (2014), we define a parameter as practically identifiable if we can constrain its value to a reasonably small region of parameter space, *i.e.*, the posterior distribution has compact support.

The estimated marginal posterior distributions (presented in Fig. 18) have a bell-like shape, with a unique, well-defined, maximum for most parameters. However, the posterior distributions for parameters K_1 and K_2 have a broad support and tend to flatten at large values, where K_1 (or K_2) > 1. This indicates greater uncertainty in the estimation of K_1 and K_2. From Eq. (8a), we note that K_1 and K_2 are only relevant in data from experiment E_2 (i.e., when oxygen levels c are above the threshold c^*). If we consider, for example, the first time at which this happens (*i.e.*, time $t_1^{(R)} = 2$ hr), then, over the period $t_1^{(R)} = 2$ hr $< t < t_2^{(H)} = 4$ hr, $Q_i(t) \approx 0$ and the evolution of $C_1(t)$ (and similarly $C_2^{(b)}$) can be determined explicitly by solving Eq. (17b) to obtain:

$$C_1(t) = C_1(t_1^{(R)})e^{-K_1(t-t_1^{(R)})}, \quad t \in (t_1^{(R)}, t_2^{(H)}). \tag{27}$$

Thus, when the first measurement is taken, $C_1(t_2^{(H)}) = C_1(t_1^{(R)})e^{-2K_1}$. If $K_1 > 1$, then $e^{-2K_1} \ll 1$ as the compartment C_1 rapidly empties after re-oxygenation. Therefore, unless C_1 is very large, $C_1(t_2^{(H)}) \approx 0$ independently of the specific value of $K_1 > 1$. In order to resolve the dynamics at this fast time-scale we would need to collect experimental data at an earlier time point, say t^*, for which $t^* - t_1^{(R)} < K_1^{-1}$; alternatively, we could choose an oxygen cycle for which a larger number of cells accumulate in the C_1 compartment. This could be achieved by prolonging the period for which the cells are exposed to severe hypoxia (i.e., $c < c^*$). While the same argument holds for K_2, since only a small number of cells enter the $C_2^{(b)}$ compartment during RH, we expect the estimation of K_2 to be more difficult since it is associated with the dynamics of a small number of cells in the total population.

7. Model predictions in the presence of uncertainty

To conclude, we use the calibrated model from §6 to make predictions on cell-cycle dynamics in different environmental conditions. We start by considering the oxygen cycles in Fig. 13 but now account for uncertainty in our parameter estimates.

For the 2hr + 6.5hr cycle in Fig. 19(a), in the absence of uncertainty, we predicted a systematic increase in the fraction of cells in S phase, with no activation of the $C_2^{(a)}$ compartment (see Fig. 13(a)). When uncertainty is taken into account, we find large variability in model predictions at longer times ($t > 25$ hr). In particular, the 68%-confidence interval encompasses the possibility of $f_s(t)$ both increasing or decreasing when $t \gg 1$ compared to its initial values. Further, activation of $C_2^{(a)}$ cannot be ruled out, as indicated by the value of $f_2(80)$, which ranges between $0 \lessapprox f_2(80) \lessapprox 0.7$ (see Fig. 19(a.3)). Despite the large uncertainty in the value of $f_2(t)$, the confidence interval on $f_1(t)$ remains reasonably small. We observe similar behaviour for cycles with a longer re-oxygenation phase (see 2hr + 8hr cycle in Fig. 19(b)). Again, uncertainty in f_s and f_2 increases over time, even though it is less pronounced than in Fig. 19(a). The 68%-confidence interval allows for the possibility of activation of the $C_2^{(a)}$ checkpoint (see increase in f_2 as $t \gg 1$) even though this is less probable than in the scenario depicted by Fig. 19(a). For both oxygen cycles considered, the uncertainty in the cell-cycle distribution is reflected in the predictions for the number of cells $N(t)$ (see Fig. 20). This is particularly evident in Fig. 20(a) where $N(80)$, the number of cells at the final time, $t = 80$ hr, ranges between $2.0 \lessapprox N(80) \lessapprox 12.5$.

Based on the results in Fig. 19, we conclude that we can use our calibrated model to predict cell-cycle dynamics on short time scales ($0 < t < 25$ hr); thereafter the increased uncertainty pre-

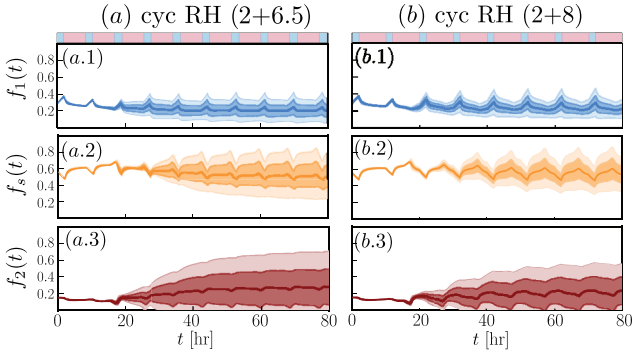

Fig. 19. Posterior estimates for the cell fractions f_m for the two cyclic protocols considered in Fig. 13: (a) cyclic RH with 2 hr in RH + 6.5 hr in an oxygenated environment; (b) cyclic RH with 2 hr in RH + 8 hr in an oxygenated environment. We plot mean estimates and indicate the 68%- and 95%-confidence intervals by the shaded regions.

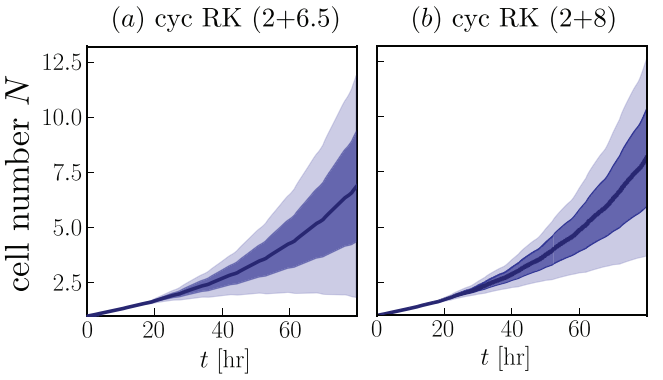

Fig. 20. Posterior estimates for the total cell number $N(t)$ for the two cyclic protocols in Fig. 19: (a) cyclic RH with 2 hr in RH + 6.5 hr in an oxygenated environment; (b) cyclic RH with 2 hr in RH + 8 hr in an oxygenated environment. We plot mean estimates and indicate the 68% and 95%-confidence intervals by the shaded regions.

vents us from making reliable predictions for the cell-cycle distribution. However, the predicted uncertainty is still informative when considering experimental design. In this case, the objective is twofold. On the one hand, we want to identify experiments that could facilitate model validation. From this point of view, we focus on times at which the uncertainty in our predictions is small (e.g., on the short time scale for experiments in Fig. 19). On the other hand, we aim also to propose experiments that could improve the accuracy of model parameter estimates. In this case, our attention focuses on scenarios where uncertainty in the model predictions is large and, therefore, new measurements can refine parameter estimates (such as for the long time dynamics in Fig. 19). From this point of view, a scenario like Fig. 19(a) is adequate since it can account for both the validation and refinement steps. Our model also suggests that, if such experiments were performed, information about the total number of cells $N(t)$ may improve model calibration, given the large variation predicted in its value at the end of the protocol.

Experimentally, it might be difficult to study scenarios for which oxygen levels change on timescales faster than two hours due to the time required for oxygen levels to equilibrate *in vitro* (Place et al., 2017). This, however, is not a limitation of our model. Indeed, we can consider what happens when a 4 hr cycle (as in E_2) is split into asymmetric periods of RH and re-oxygenation by setting $t_i^{(R)} = t_i^{(H)} + t_a$ and $t_i^{(H)} = 4(i-1)$ in Eq. (21), where $t_a \in (0,4)$. If $t_a > 2$, then the cells spend more time exposed to low oxygen levels ($c < c^*$) than to normal values ($c > c^*$); the opposite holds when $0 < t_a < 2$. As illustrated in Fig. 21(a), we ran numerical simulations up to $t = 100$ hr, during which cells were exposed to cyclic RH for the first 28 hr and then reoxygenated at constant 2% O_2. We report predictions of the true cell fractions, f_m with $m \in \{1, s, 2\}$ and total cell number, N, at 8 time points.

The results from these numerical simulations are summarised in Fig. 21. Focusing for the moment on the first 28 hr when cells are exposed to cyclic RH, we observe that, at all time points considered, the larger the value of t_a the lower is the total number of cells, N (see Fig. 21(e)). When $t_a = 2.5$ hr (see light green dots), DNA synthesis is so slow during cyclic RH that at $t = 28$ hr only a small fraction of cells has completed duplication and entered the G2/M phase. As a result, the fraction f_s is larger than for the smaller values of t_a and the fraction f_2 is smaller. In this case, during the cyclic RH phase, the variability in the model predictions remains small (even smaller than for the case $t_a = 2$ hr, which was used for the *in vitro* experiments). Therefore, our model predicts that, on short

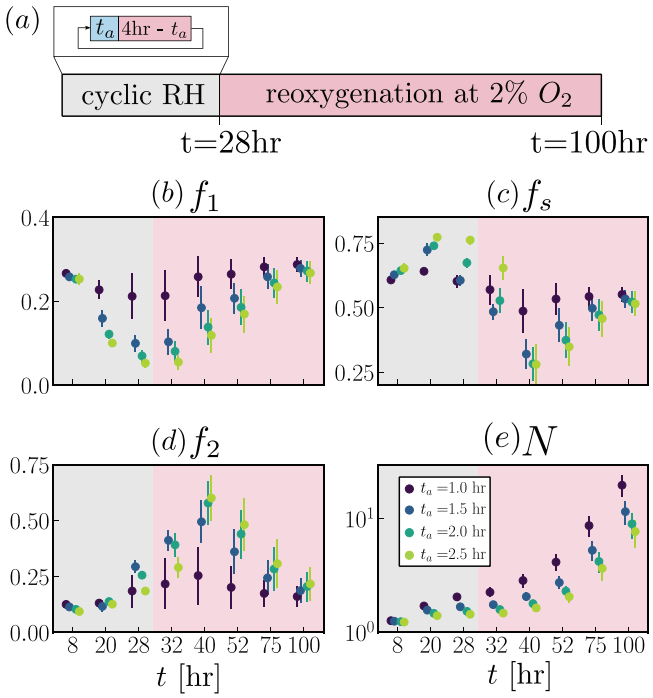

Fig. 21. Numerically-estimated values of the cell fractions f_m and cell number N for different cyclic protocols. (a) Schematic illustrating the oxygen protocols used in the numerical simulations. (b)-(e) We report posterior estimates for the model variables at 8 time points: 3 in the cyclic phase (see grey shaded area) and 5 in the reoxygenation phase (see light pink area); for each variable we report the expected value based on the estimated posterior (coloured dots) and the corresponding 68%-confidence interval indicated by the vertical lines. Different colours correspond to different oxygen dynamics, *i.e.*, a different choice of t_a (see panel (a) for the definition of t_a).

time scales (≈ 28 hr), cycles with larger t_a values favour cell accumulation in the S phase. In particular, exposing cells to cycles with $t_a = 2.5$ hr for 20 hr may be sufficient to synchronise them in the S phase of the cell-cycle. By contrast, when we decrease the value of t_a, our model predicts only a 5% increase in the fraction of cells in S phase. We note, however, that for smaller values of t_a (e.g., $t_a = 1$ hr or $t_a = 1.25$ hr), there is greater uncertainty in the predictions of f_1 and f_2 at $t = 28$ hr, due to the uncertainty in whether the $C_2^{(a)}$ checkpoint will be activated or not (results not shown). This, again, hints at the need to refine our parameter estimates by performing new experiments (such as the cycle experiment in Fig. 19) to obtain more accurate predictions for environmental conditions that deviate from those used here to calibrate our model. From this point of view, we notice that, overall, uncertainty increases after cells are reoxygenated (i.e., $t > 28$ hr). This suggests that reoxygenation experiments might be more helpful for parameter inference rather than prolonged exposure to cyclic RH. Focusing on cell fractions f_1, f_s and f_2, we notice that uncertainty in the predictions increases after reoxygenation up to $t \approx 40$ hr. For $t > 40$ hr, the cell-cycle distribution tends to relax back to the PSS solution (see §4) so that at the population level the memory of exposure to cyclic hypoxia disappears. On the contrary, we note that uncertainty in the total number of cells monotonically increases after reoxygenation. This is because, after being reoxygenated for a sufficiently long time, the cell population grows exponentially and so does the uncertainty in its predictions. We note further that, over time, differences in the cell number N associated with different values of t_a also increase, serving as a signature of the different cell-cycle dynamics during exposure to cyclic RH.

8. Discussion and future work

In this paper, we have presented a five-compartment model for the cell-cycle which accounts for cell response to variable oxygen levels. We have focused on the impact of dNTP shortages (in conditions of radio-biological hypoxia) on rates of DNA synthesis. This was achieved by introducing a variable rate, $v(t)$, of DNA synthesis and allowing transient cell-cycle arrest in the late G1 and G2 phases by transition to two checkpoint compartments: C_1 and $C_2^{(b)}$, respectively. A second checkpoint compartment, $C_2^{(a)}$, accounts for cell-cycle arrest in the G2 phase due to accumulation of replication stress and damage. Under constant oxygen-rich conditions the model reduces to a linear, three-compartment model and analytic expressions for the long time dynamics can be derived (see §4). This analysis predicts that, in the absence of competition, cells evolve to a regime of balanced exponential growth, a result which is consistent with other cell-cycle models (Basse et al., 2003; Basse et al., 2005; Begg et al., 2008; Crivelli et al., 2012; Simms et al., 2012). The main novelty of our work is the investigation of the cell-cycle dynamics in cyclic hypoxia (see §5). We show first that the model can recapitulate the experimental data from Bader et al. (2021). We then explore different oxygen dynamics and, in so doing, show different ways in which cyclic hypoxia can disregulate cell-cycle dynamics and lead to a redistribution of cells across the phases of the cell-cycle. This is of relevance when thinking about cell-cycle specific treatment, for which changes in cell-cycle distribution (even if they are transient), can have a large impact on treatment efficacy. Further, we identify scenarios in which cyclic hypoxia leads to almost complete inhibition of proliferation, and scenarios in which proliferation is only slightly slowed down. In order to use our model as a predictive tool, accurate and robust predictions are needed. In the remainder of the paper, we therefore showed how our modelling framework can be used to predict cell-cycle dynamics and inform the design of *in vitro* experiments (see §3). We started by deriving a class of candidate models ($\mathbb{M}$) based on Eqs. (17) by systematically decreasing model complexity (i.e., the number of unknown parameters). Here our aim was to test different assumptions on the mechanisms driving cell response to cyclic hypoxia. In §6, we used Bayesian model selection to identify the best candidate model amongst the ones proposed and showed that this model can indeed recapitulate the dynamic data from Bader et al. (2021). Furthermore, by constructing a class of models and applying Bayesian modelling selection, we were able to systematically show that the inclusion of the C_1 and $C_2^{(a)}$ compartments is necessary to capture the experimentally observed cell-cycle dynamics. We find, however, that the checkpoint compartment $C_2^{(b)}$ is not essential and can be neglected without significantly impacting the agreement between the model and the data. These results suggest memory effects, instead of an instantaneous response to oxygen levels, drive cell arrest in G2/M under acute exposure to cyclic RH. According to our model, damage accumulated prior to entering the G2 phase determines later arrest in this phase. In §7, we used our calibrated model to revisit the results from §5 where we account for uncertainty in parameter estimates. While the model makes precise predictions on short time scales ($t \approx 30$ hr), we observed a large uncertainty in the cell-cycle dynamics at longer times. We therefore discussed how our model could be used to inform the efficient and effective design of future experiments to refine our parameter estimates, as well as to validate predictions of the calibrated model.

In this work we showed that our model can recapitulate the response to cyclic hypoxia of a specific cancer cell line (i.e., RKO cancer cell line). For this cell line, our model predicts that both constant and cyclic radio-biological hypoxia (RH) perturb the cell-cycle dynamics, but in different ways. In constant RH, cells tend to accumulate in the late G1 phase and proliferation is rapidly halted. During cyclic RH, we predict, instead, a more diverse range of responses depending on the oxygen dynamics. We can identify regimes where proliferation is inhibited due to accumulation of cells in the G2/M phase. By contrast, when the duration of the re-oxygenation phase is increased, population growth is only mildly slowed down and the fractions of cells in the S phase is up-regulated. Additional data are needed to test whether our findings can be generalised to other cell lines and how much variability there is in their response to similar cyclic protocols. Nonetheless, based on these observations, an interesting future research direction emerges, namely, investigating the role that cyclic RH can have on the response to cell-cycle dependent treatment, such as radiotherapy. Given that cyclic RH can change the distribution of cells in the different phases of the cell-cycle, we expect a differential response to radiotherapy. This could be investigated by extending our model to include radiotherapy and to account for changes in radio-sensitivity in different phases of the cell-cycle. From this point of view, a natural question is whether cell-cycle redistribution is sufficient to explain the increase in radio-resistance due to cyclic hypoxia, as reported in the literature (Hines et al., 2014; Hsieh et al., 2010; Hsieh et al., 2012).

In this paper, our focus was on constructing a minimal model to describe the influence of cyclic hypoxia on the cell-cycle, which could be validated against existing experimental data. This guided our assumption that the rates $\mathscr{R}_\pm$ at which cells adjust their rate of DNA synthesis, v, to be constant. In practice, $\mathscr{R}_\pm$ may also depend on the level of damage and replication stress accumulated by the cell during cyclic hypoxia. Our model could easily be extended to account for these effects, but at the cost of increasing the number of unknown model parameters. *In silico* hypothesis testing (using a Bayesian framework, as in §6), could be used to compare different modelling assumptions (i.e., constant vs variable rates), and to investigate the design of future experiments that can distinguish between alternative mathematical models.

In several instances we have mentioned that DNA damage plays a key role in mediating cell-cycle progression and cell-cycle arrest in cyclic hypoxia. However, for simplicity, we have accounted for it only implicitly. In principle, our model could be extended by introducing DNA damage as an additional structural variable to describe cell state. Introducing DNA damage into the model would enable us to account for radiotherapy in a more realistic manner. Analogously to re-oxygenation, radiotherapy also causes DNA damage. Such a model extension could be used to investigate whether cyclic hypoxia selects for radio-resistant clones which are less sensitive to damage accumulation. Further model extensions could account for spatial heterogeneity, and bring the model closer to *in vivo* conditions. In this light, we view our work as a first step towards developing a theoretical framework for investigating cyclic hypoxia and its effect on cell-cycle progression, particularly in the context of solid tumours.

Funding

G.L.C. is supported by EPSRC and MRC Centre for Doctoral Training in Systems Approaches to Biomedical Science (GRANT_NUMBER: EP/L016044/1) and Cancer Research UK.

CRediT authorship contribution statement

Giulia L. Celora: Conceptualization, Methodology, Software, Formal analysis, Visualization, Writing - original draft, Writing - review & editing. **Samuel B. Bader:** Conceptualization, Investigation. **Ester M. Hammond:** Conceptualization, Writing - original draft, Writing - review & editing, Supervision. **Philip K. Maini:**

Conceptualization, Writing - original draft, Writing - review & editing, Supervision. **Joe M. Pitt-Francis:** Conceptualization, Writing - original draft, Writing - review & editing, Supervision. **Helen M. Byrne:** Conceptualization, Writing - original draft, Writing - review & editing, Supervision.

Data Availability statement

In compliance with EPSRC's open access initiative, the research materials supporting this publication can be accessed by contacting celora@maths.ox.ac.uk.

Declaration of Competing Interest

The authors declare that they have no known competing financial interests or personal relationships that could have appeared to influence the work reported in this paper.

Appendix A. Exponential steady state uniqueness

Starting from Eqs. (19), we note that the evolution of the number of cells, N, decouples from the equations for G_1 and G_2 so that we can consider the reduced model:

$$\frac{dG_1}{dt} = 2k_2G_2 - k_1G_1, \tag{A.1a}$$

$$\frac{dG_2}{dt} = -k_2G_2 + k_1G_1(t-\tau_s). \tag{A.1b}$$

Since Eqs. (A.1) form a system of linear delay differential equations, their solutions can be written as a superposition of exponential functions $e^{\Lambda t}$ with corresponding eigenvalues $\Lambda \in \mathbb{C}$. We therefore know that the long time behaviour of the system will be dominated by the eigenvalue Λ with largest real part, here denoted by λ. Unlike for ordinary differential equations, the number of eigenvalues Λ for a delay differential equation is infinite and they are defined by the characteristic equation:

$$\det(A(\Lambda) - \Lambda\mathbb{I}) = 0, \quad A(\Lambda) = \begin{bmatrix} -k_1 & 2k_2 \\ k_1e^{-\Lambda\tau_s} & -k_2 \end{bmatrix} \tag{A.2}$$

where $\mathbb{I}$ is the identity matrix in $\mathbb{R}^{2\times 2}$. Evaluating the determinant explicitly we obtain the following transcendental equation, whose roots correspond to the eigenvalues Λ of Eqs. (A.1):

$$P(\Lambda) \equiv -(\Lambda + k_1)(\Lambda + k_2) + 2k_1k_2e^{-\Lambda\tau_s} = 0. \tag{A.3}$$

It can be shown that this system has at least one root with $\mathrm{Re}(\Lambda) > 0$ so that the solution will blow up in time, i.e. $\lim_{t\to\infty} G_1, G_2 = \infty$. We also have that the spectrum of eigenvalues is bounded above, in the sense that there exists an upper limit to the values of $\mathrm{Re}(\Lambda)$. This is analogous to the system investigated by Crivelli et al. (2012). Lemma 1 summarises some of their results as adapted to our model.

Lemma 1. For any value of $k_1 > 0, k_2 > 0$ and $\tau_s > 0$, the rightmost root of $P(\Lambda)$ as defined by Eq. (A.3) is real and positive.

Proof. Let us first consider the existence of a real and positive root $\Lambda = \Lambda_0$. This is straightforward to prove since $P(\Lambda)$ is continuous and $P(0) > 0$, while $\lim_{\Lambda\to\infty} P(\Lambda) < 0$. Given that for $\Lambda > 0$, $dP/d\Lambda < 0$, i.e. P is strictly monotonically decreasing, we have that the zero $\Lambda = \Lambda_0$ is unique. This implies that for any choice of parameters, the trivial steady state $(0,0)$ is unstable.

Let us now consider the complex solution $\Lambda = \Lambda_R + i\Lambda_I$ for the function P, where $\Lambda_I \in \mathbb{R}\setminus\{0\}$:

$$(\Lambda_R + i\Lambda_I + k_1)(\Lambda_R + i\Lambda_I + k_2) = 2k_1k_2e^{-(\Lambda_R + i\Lambda_I)\tau_s}. \tag{A.4}$$

Taking absolute values of the above we obtain that:

$$\begin{aligned} &2k_1k_2e^{-\Lambda_R\tau_s} = \sqrt{((\Lambda_R + k_1)^2 + \Lambda_I^2)((\Lambda_R + k_2)^2 + \Lambda_I^2)} \\ &\Rightarrow 2k_1k_2e^{-\Lambda_R\tau_s} > (\Lambda_R + k_1)(\Lambda_R + k_2), \end{aligned} \tag{A.5}$$

which implies that $P(\Lambda_R) > 0 = P(\Lambda_0)$, where Λ_0 is the unique real root of $P(\Lambda)$. Since P is strictly monotonically decreasing, we have that $\Lambda_R < \Lambda_0$. We therefore have that the rightmost eigenvalue is real and it is positive.

Based on Lemma 1, we know that for any choice of model parameters, under unperturbed growth, cells will eventually reach a regime in which they grow exponentially. This is a common result of many cell-cycle models for *in vitro* systems and it is usually referred to as balanced, or asynchronous, exponential growth:

$$G_{1,2}(t) \approx \xi_{1,2}e^{\lambda t}, \quad t \gg 1, \tag{A.6a}$$

where $\xi_{1,2}$ are positive constants. Having characterised the long time behaviour of $G_1(t)$ and $G_2(t)$, let us discuss what this implies for the other model variables, i.e. the distribution $S(x,t)$ and the total number of cells, N. Using Eq. (9) we find that, in the case of unperturbed growth and assuming $t > \tau_s$, the long time distribution $S(x,t)$ takes the form:

$$S(x,t) \approx \tau_s k_1 \frac{\xi_1}{\xi_n} e^{-\lambda\tau_s(x-1)}\xi_n e^{\lambda t}, \quad t \gg 1, \tag{A.6b}$$

which can be written by separating the DNA and time components, as $S(x,t) \approx \bar{s}(x)\xi_n e^{\lambda t}$. This implies that the population P_s also grows exponentially, $P_s(t) = \xi_s e^{\lambda t}$ where $\xi_s = \xi_n \int_1^2 \bar{s}(x)dx$. Combining this with Eq. (A.6a), we can compute the total number of cells and the cell fractions:

$$N(t) \approx (\xi_1 + \xi_2 + \xi_s)e^{\lambda t} = \xi_N e^{\lambda t}, \quad t \gg 1, \tag{A.6c}$$

$$f_j(t) \approx \bar{f}_j = \frac{\xi_j}{\xi_N}, \quad j \in \{1, s, 2\}, \ t \gg 1. \tag{A.6d}$$

We therefore find that the long time behaviour is characterised by a stationary DNA-distribution, $\bar{s}(x)$, of cells in the S phase, and constant cell fractions, $\bar{f}_j$. Following Simms et al. (2012) we will denote this specific regime as the *phase stationary solution* to highlight the fact that the fraction of cells in each phase of the cycle remains constant.

We now discuss how this phase stationary solution of the model can be used to estimate the model parameters. Assume that the cells are left growing in an unperturbed environment for sufficiently long time so as to reach the regime of balanced exponential growth. Provided that we know the fraction of cells, $\bar{f}_j$, and proliferation rate, λ, of the population of cells (which can be approximated using the doubling time as given in the main text, $T_{doub} = \lambda^{-1}\ln 2$), we can uniquely identify the parameters k_1, k_2, τ_s in the model. Let us substitute the solution (A.6) into Eqs. (19) and, upon re-writing $G_i(t) = \bar{f}_i\xi_N e^{\lambda t}$, we obtain the following algebraic system:

$$\lambda\bar{f}_2 = -k_2\bar{f}_2 + \bar{f}_1k_1e^{-\tau_s\lambda}, \tag{A.7a}$$

$$\lambda\bar{f}_1 = 2k_2\bar{f}_2 - k_1\bar{f}_1, \tag{A.7b}$$

$$\lambda = k_2\bar{f}_2. \tag{A.7c}$$

Looking at Eq. (A.7c) it is apparent that k_2 is uniquely identified and it is positive. Substituting k_2 into Eq. (A.7b), we obtain an equation for k_1:

$$k_1 = \frac{2 - \bar{f}_1}{\bar{f}_1}\lambda, \tag{A.8}$$

where we note that $k_1 > 0$ since, by definition, $\bar{f}_1 \leq 1$. Substituting now the forms of k_1 and k_2 into (A.7a) we obtain an expression for τ_s:

$$\tau_s = \frac{1}{\lambda} \ln\left(\frac{2-\bar{f}_1}{\bar{f}_2+1}\right) \tag{A.9}$$

where the physical constraint $\bar{f}_1 + \bar{f}_2 \leq 1$ guarantees that the logarithm is always positive. Hence, given the measurements of $\bar{f}_1, \bar{f}_2$ and τ_s we can uniquely identify the constant parameters appearing in the model (19) for unperturbed growth.

Appendix B. Experimental data

Here we present the raw-data for the cell-cycle dynamics in RKO cancer cells as measured in the experiments from Bader et al. (2021) discussed in §2 of the main text. Table B.6 summarises the value of the cell fractions in normoxia (E_0), while Table B.7 and Table B.8 represent the time series data obtained when cells are exposed to constant (E_1) and cyclic (E_2) RH, respectively.

Table B.6
Raw experimental data for the stationary cell-cycle dynamics of RKO cancer cells when exposed to normoxia (E_0) for sufficiently long time.

F_1	F_s	F_2
0.291222313	0.557013946	0.151763741
0.297764120	0.533750132	0.168485748
0.276288660	0.602061856	0.121649485
0.391933816	0.475698035	0.132368149
0.270000000	0.540000000	0.190000000
0.353889645	0.498481834	0.147628521
0.296387429	0.515714126	0.187898445
0.289529012	0.571414043	0.139056945
0.291841004	0.560669456	0.147489540

Table B.7
Raw experimental data for the cell-cycle dynamics of RKO cancer cells when exposed to constant RH (E_1).

Time [hr]	F_1	F_s	F_2
4	0.491356731	0.297537978	0.207438449
4	0.497400877	0.36815819	0.131485068
8	0.513138837	0.334160977	0.147941237
8	0.563423645	0.325328407	0.104679803

Table B.8
Raw experimental data for the cell-cycle dynamics of RKO cancer cells when exposed to cyclic RH (E_2).

Time [hr]	F_1	F_s	F_2
4	0.330630725	0.546067179	0.120037907
4	0.266513378	0.632211538	0.098035117
4	0.297175141	0.534011299	0.164971751
8	0.220709571	0.731332508	0.044657591
8	0.191676374	0.754315366	0.050937202
20	0.159383033	0.702313625	0.133676093
20	0.093743547	0.777617179	0.125954987
20	0.144138373	0.711189408	0.140935298
20	0.100658314	0.726587386	0.168825653
20	0.184611856	0.635248251	0.171998624
20	0.145497026	0.713785047	0.13700085
28	0.060079664	0.712547024	0.21132994
28	0.044509303	0.647087438	0.29916089
28	0.03960499	0.676611227	0.280665281

Appendix C. MCMC sampling algorithm and results

In order to estimate the posterior distribution (see Eq. (24a)), we use Markov Chain Monte Carlo (MCMC) methods, employing the freely available implementation in the python package PINTS (Clerx et al., 2019). As suggested by Johnstone et al. (2016), prior to starting our MCMC routine, we compute a good initial guess by maximizing the likelihood function $\mathscr{L}_{\mathscr{M}}$ (see Eq. (23b)). Based on Eq. (24a) and the choice of a uniform prior, maximising the posterior is equivalent to maximising the likelihood function. Sampling random initial guesses from the prior distribution π_{pr}, we solve the optimisation problem for the log-likelihood using the `CMA-ES` algorithm (Clerx et al., 2019; Hansen et al., 2003). We then use the output of the optimization routine to initiate the MCMC simulation (we compute, in total, three chains). We sample from the posterior distribution by using `HaarioBardenetMCMC`, which is a Metropolis–Hastings algorithm with adaptive covariance, where the first 8000 iterations are performed without adaptation (as suggested by Johnstone et al., 2016). We compute up to 30000 iterations for each chain and discard the first 10000 as "*warm-up*". As in Collis et al. (2017), we assess the convergence of the MCMC chains by estimating $\widehat{R}$ (Lambert, 2018, Chapter 13), where we accept the sampled posterior if $\widehat{R} < 1.05$ (note that $\widehat{R} \to 1$ as the algorithm converges).

In Figs. 22–26, we show the estimated posterior distributions for our class of models $\mathbb{M}$ (see Table 3). Summary statistics of the marginal posterior distributions are listed in Table C.9. For the point estimates of parameter values in §5, we use the mean of the marginal posterior distributions (see Table C.9).

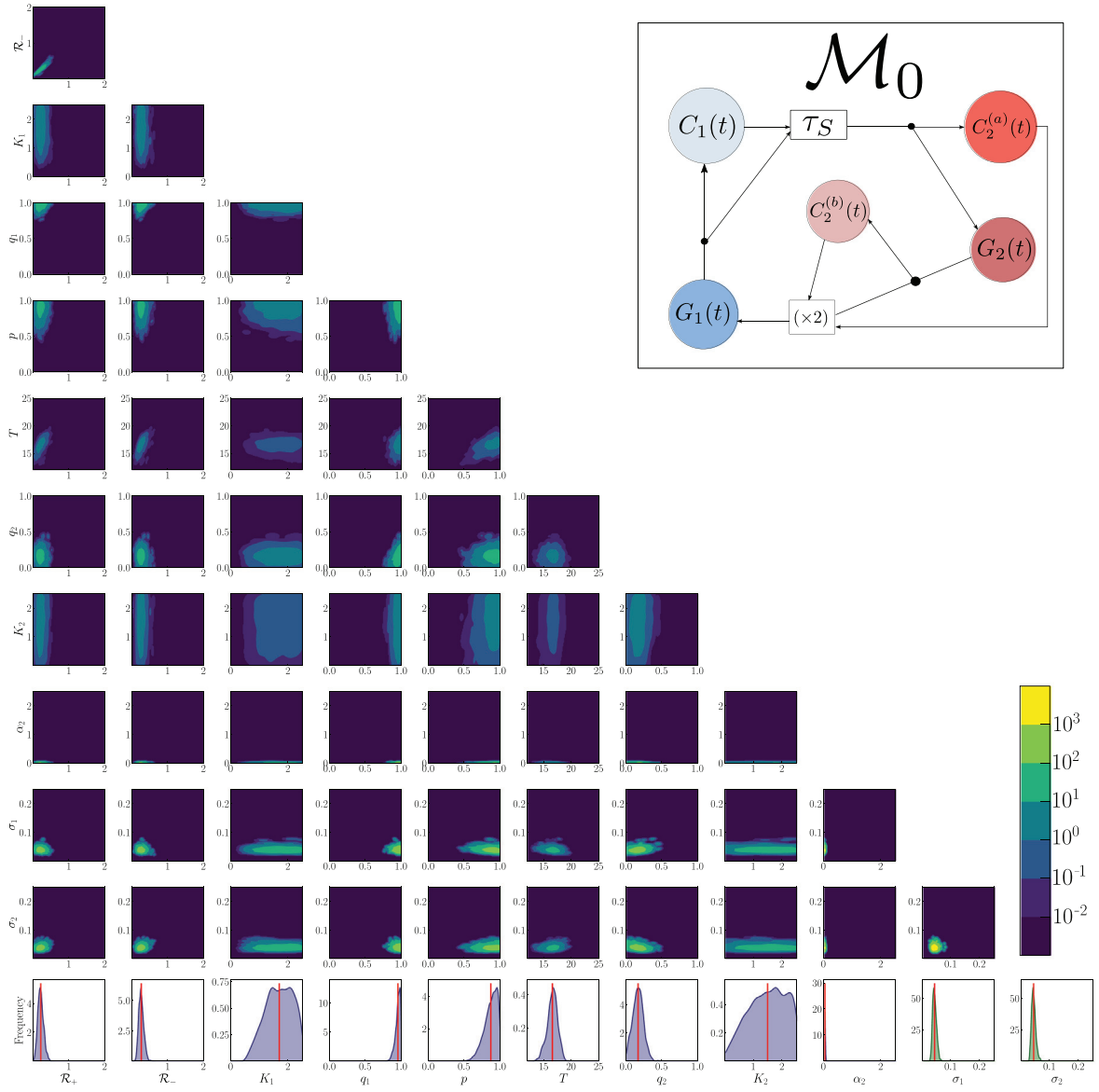

Fig. 22. Approximation of the joint (surface plot) and marginal (last row) posterior distributions for model $\mathcal{M}_0$ from Table 3 (see schematic in top-right corner). The distributions were obtained by using the MCMC samples generated as discussed in the text above. In the surface plots for the joint distributions, yellow areas correspond to high posterior probability and blue areas correspond to low probability (see colour-bar on the right). In the last row, the red vertical line indicates the mean of the marginal posterior distribution as reported in Table C.9, where additional summary statistics extrapolated from the marginal distribution are also given. Note also that in the last row the y-axes are scaled differently.

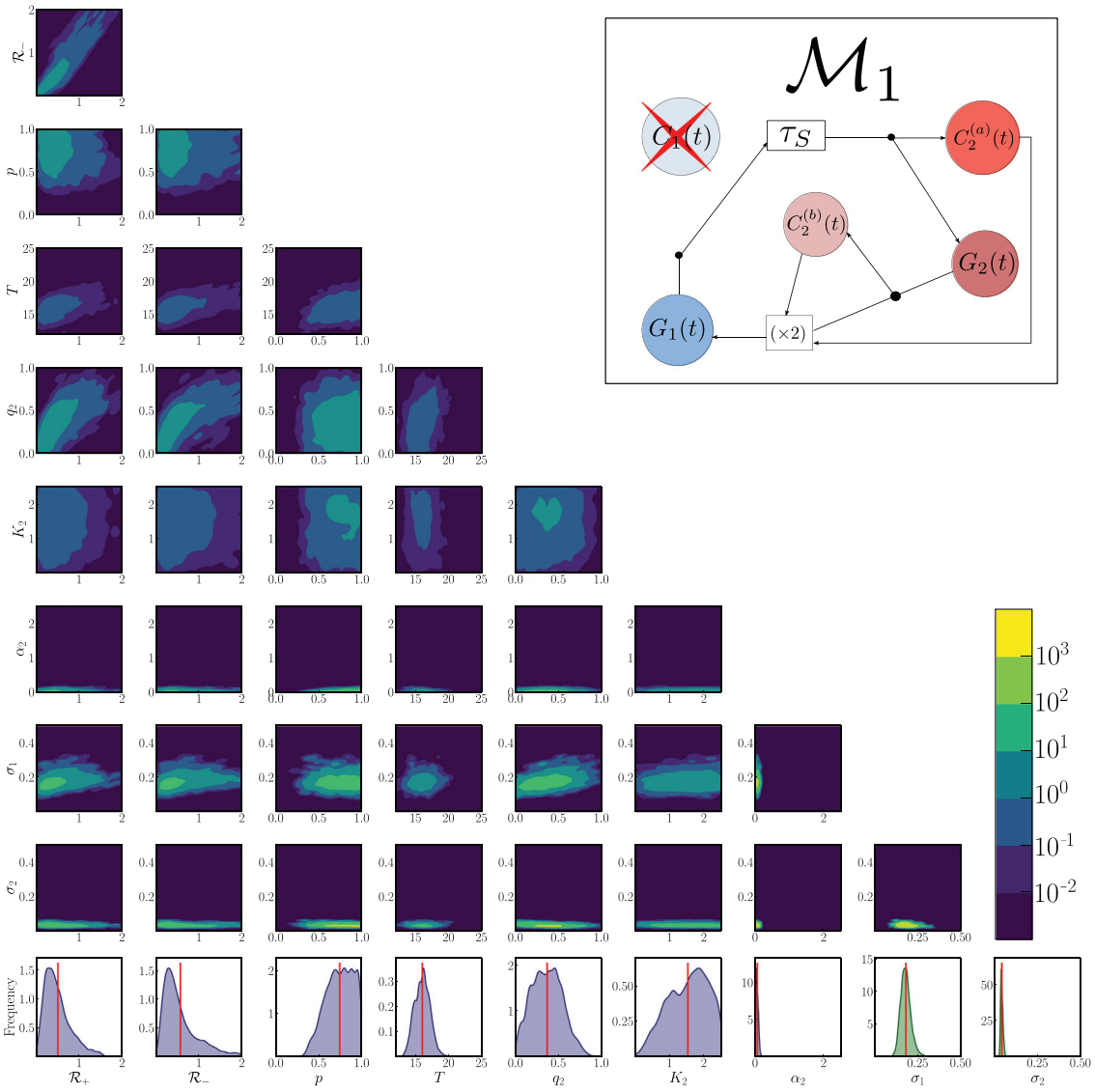

Fig. 23. Approximation of the joint (surface plot) and marginal (last row) posterior distributions for model $\mathscr{M}_1$ from Table 3 (see schematic in top-right corner). The distributions were obtained by using the MCMC samples generated as discussed in the text above. In the surface plots for the joint distributions, yellow areas correspond to high posterior probability and blue areas correspond to low probability (see colour-bar on the right). In the last row, the red vertical line indicates the mean of the marginal posterior distribution as reported in Table C.9, where additional summary statistics extrapolated from the marginal distribution are also given. Note also that in the last row the y-axes are scaled differently.

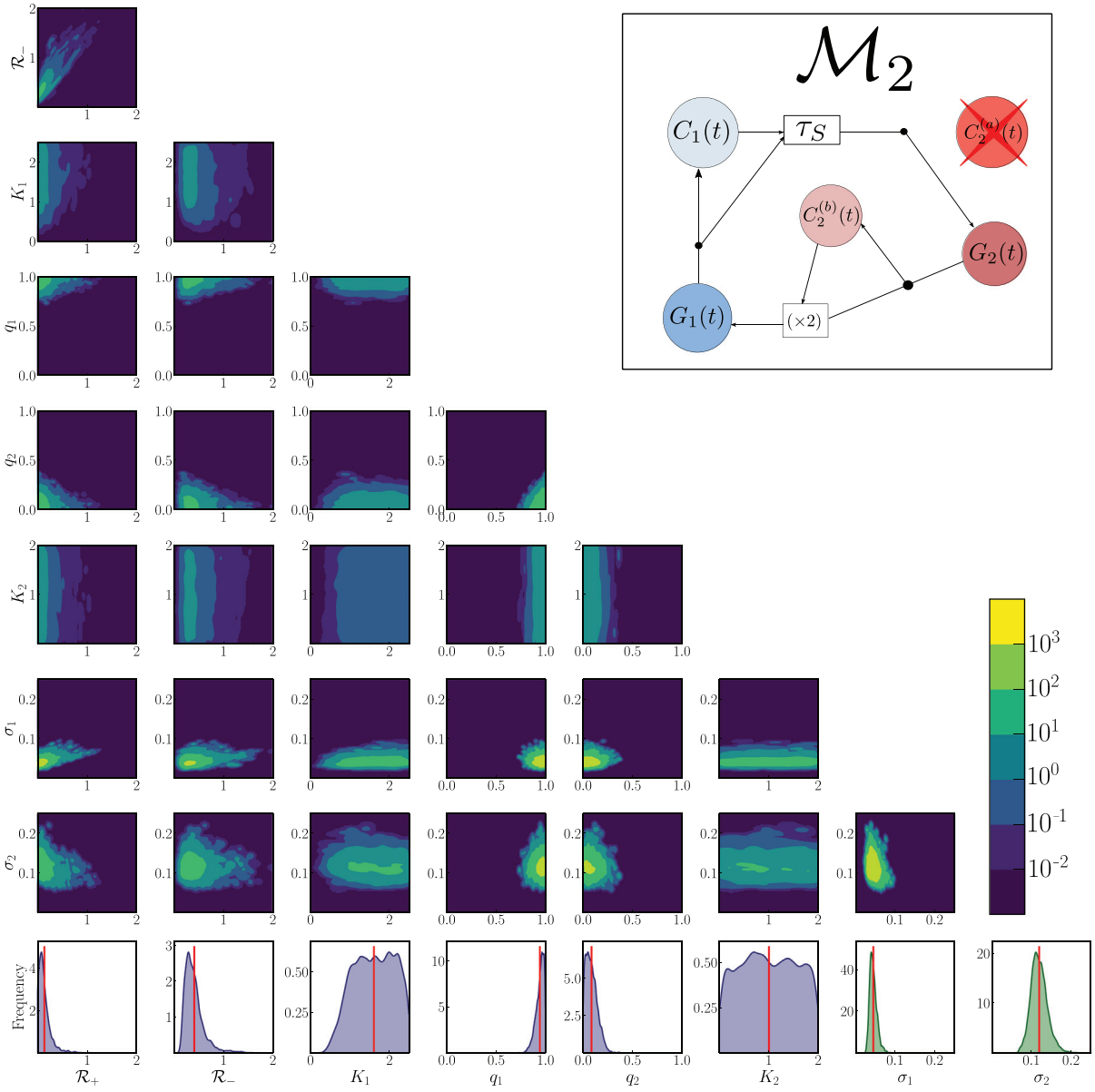

Fig. 24. Approximation of the joint (surface plot) and marginal (last row) posterior distributions for model $\mathscr{M}_2$ from Table 3 (see schematic in top-right corner). The distributions were obtained by using the MCMC samples generated as discussed in the text above. In the surface plots for the joint distributions, yellow areas correspond to high posterior probability and blue areas correspond to low probability (see colour-bar on the right). In the last row, the red vertical line indicates the mean of the marginal posterior distribution as reported in Table C.9, where additional summary statistics extrapolated from the marginal distribution are also given. Note also that in the last row the y-axes are scaled differently.

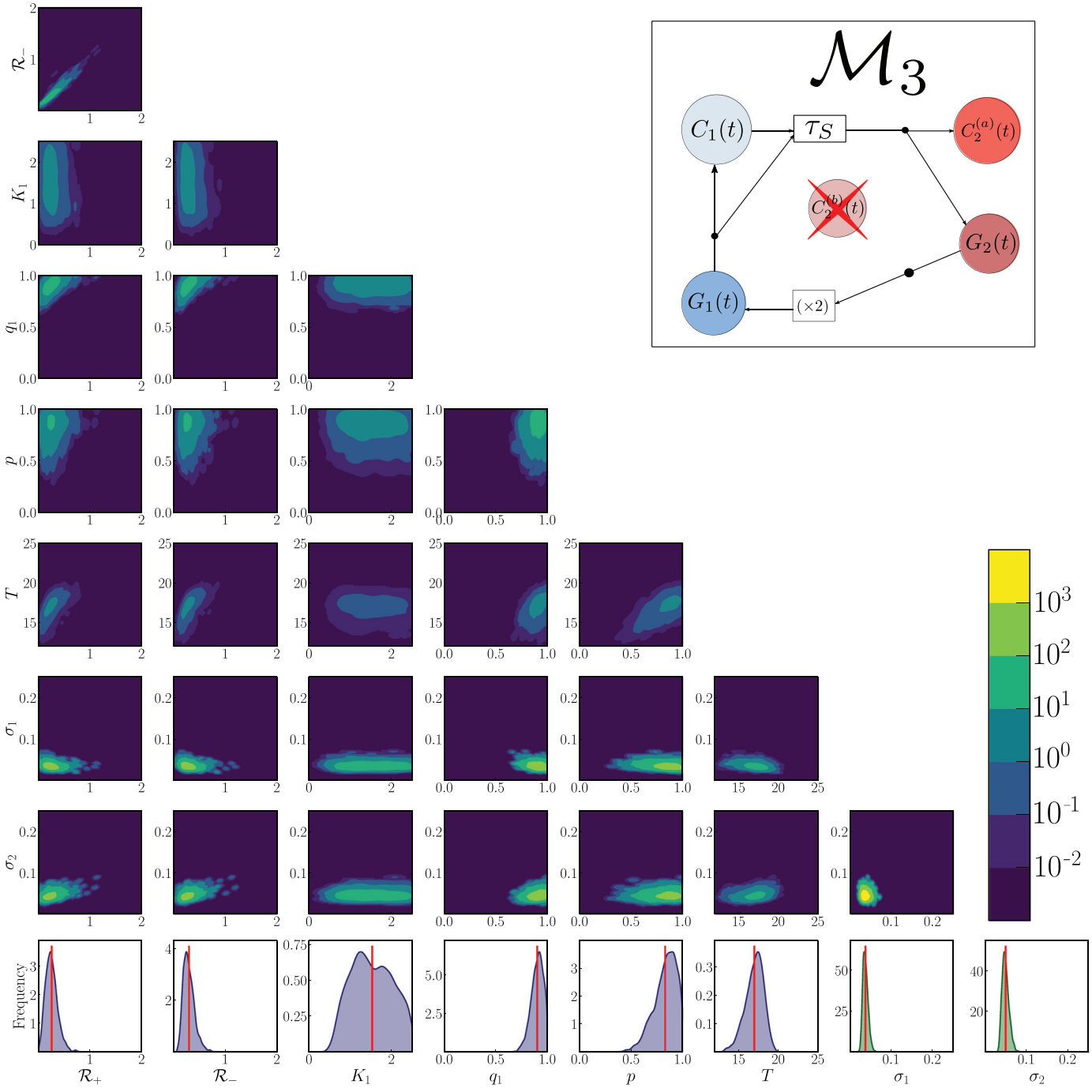

Fig. 25. Approximation of the joint (surface plot) and marginal (last row) posterior distributions for model $\mathcal{M}_3$ from Table 3 (see schematic in top-right corner). The distributions were obtained by using the MCMC samples generated as discussed in the text above. In the surface plots for the joint distributions, yellow areas correspond to high posterior probability and blue areas correspond to low probability (see colour-bar on the right). In the last row, the red vertical line indicates the mean of the marginal posterior distribution as reported in Table C.9, where additional summary statistics extrapolated from the marginal distribution are also given. Note also that in the last row the y-axes are scaled differently.

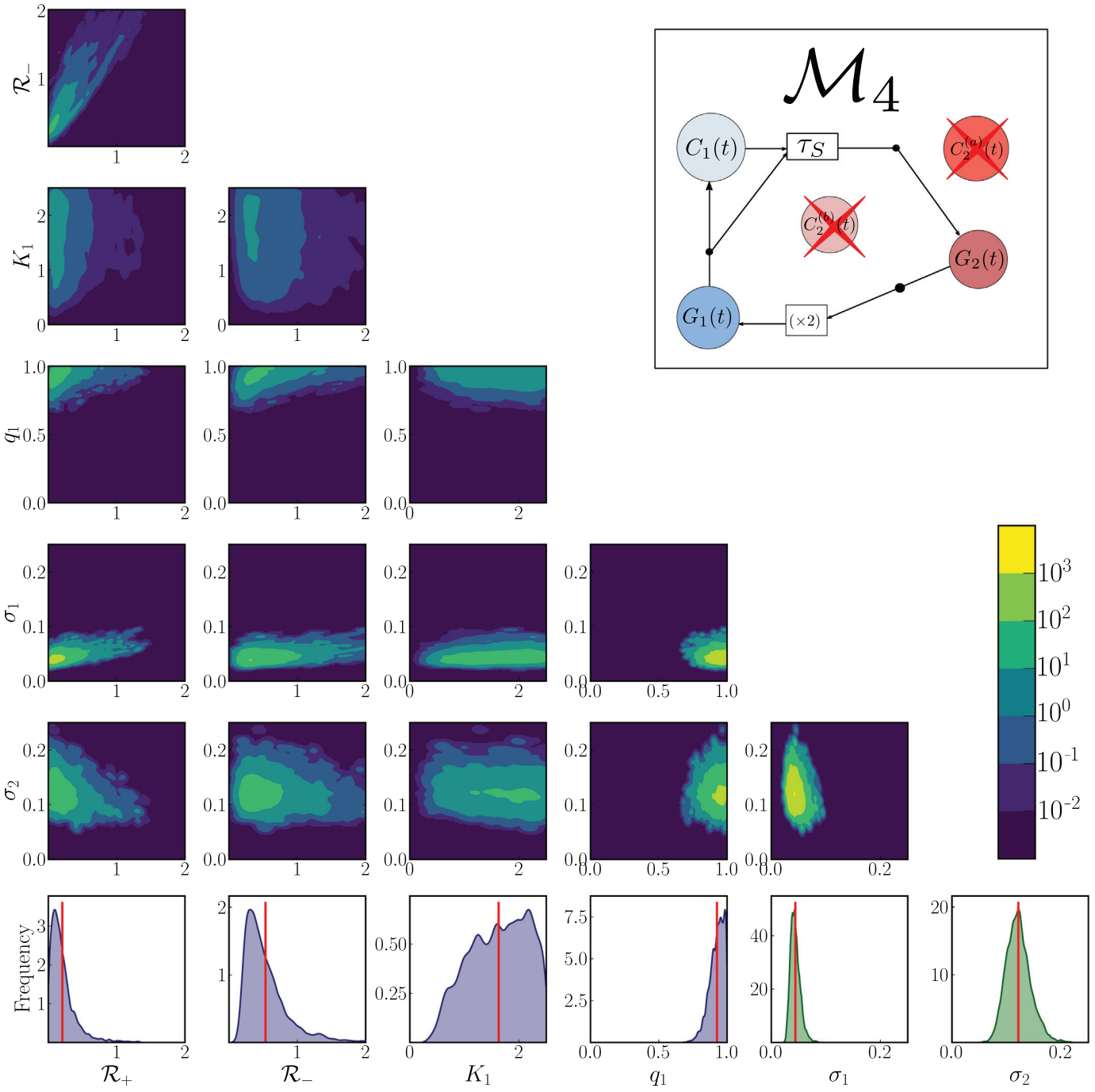

Fig. 26. Approximation of the joint (surface plot) and marginal (last row) posterior distributions for model $\mathcal{M}_4$ from Table 3 (see schematic in top-right corner). The distributions were obtained by using the MCMC samples generated as discussed in the text above. In the surface plots for the joint distributions, yellow areas correspond to high posterior probability and blue areas correspond to low probability (see colour-bar on the right). In the last row, the red vertical line indicates the mean of the marginal posterior distribution as reported in Table C.9, where additional summary statistics extrapolated from the marginal distribution are also given. Note also that in the last row the y-axes are scaled differently.

Table C.9
Summary statistics for the marginal posterior distributions for the family of models $\mathbb{M}$ listed in Table 3 in §5.2. Here we report the mean and standard deviation together with the quantiles (Q_i) of the distribution. The final column shows the value of $\hat{R}$ used to estimate the convergence of the MCMC algorithm, where convergence corresponds to $\hat{R} < 1.05$.

Model		**mean**	std	$Q_{25\%}$	$Q_{50\%}$	$Q_{75\%}$	$\hat{R}$
$\mathscr{M}_0$	$\mathscr{R}_+$	0.22	0.08	0.16	0.21	0.26	1.01
	$\mathscr{R}_-$	0.26	0.07	0.21	0.26	0.30	1.02
	K_1	1.69	0.47	1.34	1.70	2.08	1.01
	q_1	0.95	0.04	0.93	0.96	0.98	1.02
	p	0.87	0.09	0.81	0.89	0.94	1.02
	T	16.47	0.92	15.91	16.52	17.11	1.01
	α_2	0.02	0.01	0.01	0.02	0.03	1.03
	q_2	0.16	0.07	0.11	0.16	0.21	1.01
	K_2	1.48	0.64	1.00	1.53	2.03	1.01
	σ_1	0.04	0.01	0.04	0.04	0.04	1.02
	σ_2	0.04	0.01	0.04	0.04	0.04	1.01
$\mathscr{M}_1$	$\mathscr{R}_+$	0.51	0.30	0.29	0.45	0.65	1.01
	$\mathscr{R}_-$	0.55	0.35	0.29	0.46	0.72	1.02
	p	0.74	0.16	0.62	0.74	0.87	1.01
	T	15.92	1.17	15.08	15.96	16.74	1.01
	α_2	0.05	0.03	0.02	0.05	0.07	1.04
	q_2	0.37	0.17	0.24	0.36	0.49	1.02
	K_2	1.47	0.59	1.01	1.50	1.94	1.01
	σ_1	0.18	0.03	0.16	0.17	0.20	1.02
	σ_2	0.04	0.01	0.03	0.04	0.04	1.02
$\mathscr{M}_2$	$\mathscr{R}_+$	0.15	0.14	0.06	0.12	0.19	1.05
	$\mathscr{R}_-$	0.42	0.21	0.28	0.38	0.49	1.04
	K_1	1.61	0.51	1.20	1.63	2.04	1.01
	q_1	0.89	0.06	0.86	0.90	0.94	1.01
	q_2	0.08	0.06	0.04	0.08	0.12	1.02
	K_2	1.00	0.57	0.53	0.98	1.48	1.01
	σ_1	0.04	0.01	0.04	0.04	0.05	1.02
	σ_2	0.12	0.02	0.10	0.12	0.13	1.01
$\mathscr{M}_3$	$\mathscr{R}_+$	0.26	0.12	0.17	0.25	0.33	1.00
	$\mathscr{R}_-$	0.30	0.13	0.22	0.28	0.58	1.00
	K_1	1.53	0.50	1.13	1.50	1.94	1.00
	q_1	0.90	0.06	0.86	0.91	0.95	1.00
	p	0.83	0.11	0.76	0.85	0.91	1.00
	T	16.93	1.18	16.21	17.05	17.78	1.00
	σ_1	0.04	0.01	0.03	0.04	0.04	1.00
	σ_2	0.05	0.01	0.04	0.05	0.05	1.00
$\mathscr{M}_4$	$\mathscr{R}_+$	0.21	0.19	0.08	0.16	0.27	1.04
	$\mathscr{R}_-$	0.53	0.31	0.32	0.45	0.66	1.03
	K_1	1.63	0.53	1.22	1.66	2.08	1.01
	q_1	0.93	0.05	0.89	0.93	0.97	1.01
	σ_1	0.04	0.01	0.04	0.04	0.05	1.01
	σ_2	0.12	0.02	0.11	0.12	0.14	1.01

References

Alarcón, T., Byrne, H.M., Maini, P.K., 2004. A mathematical model of the effects of hypoxia on the cell-cycle of normal and cancer cells. J. Theor. Biol. 229, 395–411. https://doi.org/10.1016/j.jtbi.2004.04.016.

Alfieri, R., Bartocci, E., Merelli, E., Milanesi, L., 2011. Modeling the cell cycle: From deterministic models to hybrid systems. BioSystems 105, 34–40. https://doi.org/10.1016/j.biosystems.2011.03.002.

Altinok, A., Gonze, D., Lévi, F., Goldbeter, A., 2011. An automaton model for the cell cycle. Interface Focus 1, 36–47. https://doi.org/10.1098/rsfs.2010.0009.

Bader, S.B., Dewhirst, M.W., Hammond, E.M., 2021. Review cyclic hypoxia: An update on its characteristics, methods to measure it and biological implications in cancer. Cancers 13, 1–20. https://doi.org/10.3390/cancers13010023.

Bader, S.B., Ma, T.S., Simpson, C.J., Liang, J., Maezono, S.E.B., Olcina, M.M., Buffa, F.M., Hammond, E.M., 2021. Replication catastrophe induced by cyclic hypoxia leads to increased APOBEC3B activity. Nucleic Acids Res. 49, 7492–7506. https://doi.org/10.1093/nar/gkab551.

Barker, H., Paget, J., Khan, A., Harrington, K., 2015. The tumour microenvironment after radiotherapy: Mechanisms of resistance and recurrence. Nature Rev. Cancer 15, 409–425. https://doi.org/10.1038/nrc3958.

Bartkova, J., Horejší, Z., Koed, K., Krämer, A., Tort, F., Zleger, K., Guldberg, P., Sehested, M., Nesland, J.M., Lukas, C., Orntoft, T., Lukas, J., Bartek, J., 2005. DNA damage response as a candidate anti-cancer barrier in early human tumorigenesis. Nature 434, 864–870. https://doi.org/10.1038/nature03482.

Basse, B., Baguley, B.C., Marshall, E.S., Joseph, W.R., Van Brunt, B., Wake, G., Wall, D. J., 2003. A mathematical model for analysis of the cell cycle in cell lines derived from human tumors. J. Math. Biol. 47, 295–312. https://doi.org/10.1007/s00285-003-0203-0.

Basse, B., Baguley, B.C., Marshall, E.S., Joseph, W.R., Van Brunt, B., Wake, G., Wall, D. J., 2004. Modelling cell death in human tumour cell lines exposed to the anticancer drug paclitaxel. J. Math. Biol. 49, 329–357. https://doi.org/10.1007/s00285-003-0254-2.

Basse, B., Baguley, B.C., Marshall, E.S., Wake, G.C., Wall, D.J., 2005. Modelling the flow of cytometric data obtained from unperturbed human tumour cell lines: Parameter fitting and comparison. Bull. Math. Biol. 67, 815–830. https://doi.org/10.1016/j.bulm.2004.10.003.

Basse, B., Ubezio, P., 2007. A generalised age- and phase-structured model of human tumour cell populations both unperturbed and exposed to a range of cancer therapies. Bull. Math. Biol. 69, 1673–1690. https://doi.org/10.1007/s11538-006-9185-6.

Begg, K., Tavassoli, M., 2020. Inside the hypoxic tumour: reprogramming of the DDR and radioresistance. Cell Death Discovery 6, 1234567890. https://doi.org/10.1038/s41420-020-00311-0.

Begg, R.E., Wall, D.J., Wake, G.C., 2008. The steady-states of a multi-compartment, age-size distribution model of cell-growth. European J. Appl. Math. 19, 435–458. https://doi.org/10.1017/S0956792508007535.

Bell, G.I., 1968. Cell growth and division: III. Conditions for balanced exponential growth in a mathematical model. Biophys. J. 8, 431–444. https://doi.org/10.1016/S0006-3495(68)86498-7.

Bristow, R.G., Hill, R.P., 2008. Hypoxia and metabolism: Hypoxia, DNA repair and genetic instability. Nat. Rev. Cancer 8, 180–192. https://doi.org/10.1038/nrc2344.

Chao, H.X., Poovey, C.E., Privette, A.A., Grant, G.D., Chao, H.Y., Cook, J.G., Purvis, J.E., 2017. Orchestration of DNA Damage Checkpoint Dynamics across the Human Cell Cycle. Cell Syst. 5, 445–459.e5. https://doi.org/10.1016/j.cels.2017.09.015.

Chapman, S.J., Plank, M.J., James, A., Basse, B., 2008. A nonlinear model of age and size-structured populations with applications to cell cycles. ANZIAM J. 49, 151–169. https://doi.org/10.1017/S144618110001275X.

Chiorino, G., Lupi, M., 2002. Variability in the timing of G1/S transition. Math. Biosci. 177–178, 85–101. https://doi.org/10.1016/S0025-5564(02)00085-8.
Clerx, M., Robinson, M., Lambert, B., Lei, C.L., Ghosh, S., Mirams, G.R., Gavaghan, D.J., 2019. Probabilistic inference on noisy time series (PINTS). J. Open Res. Software 7, 23. https://doi.org/10.5334/jors.252.
Collis, J., Connor, A.J., Paczkowski, M., Kannan, P., Pitt-Francis, J., Byrne, H.M., Hubbard, M.E., 2017. Bayesian Calibration, Validation and Uncertainty Quantification for Predictive Modelling of Tumour Growth: A Tutorial. Bull. Math. Biol. 79, 939–974. https://doi.org/10.1007/s11538-017-0258-5.
Crivelli, J.J., Földes, J., Kim, P.S., Wares, J.R., 2012. A mathematical model for cell cycle-specific cancer virotherapy. J. Biol. Dyn. 6, 104–120. https://doi.org/10.1080/17513758.2011.613486.
Csikász-Nagy, A., 2009. Computational systems biology of the cell cycle. Briefings Bioinform. 10, 424–434. https://doi.org/10.1093/bib/bbp005.
Daly, A.C., Gavaghan, D., Cooper, J., Tavener, S., 2018. Inference-based assessment of parameter identifiability in nonlinear biological models. J. R. Soc. Interface 15, 20180318. https://doi.org/10.1098/rsif.2018.0318.
Ducrot, A., Le Foll, F., Magal, P., Murakawa, H., Pasquier, J., Webb, G.F., 2011. An in vitro cell population dynamics model incorporating cell size, quiescence, and contact inhibition. Math. Models Methods Appl. Sci. 21, 871–892. https://doi.org/10.1142/S0218202511005404.
Fadda, S., Cincotti, A., Cao, G., 2012. A novel population balance model to investigate the kinetics of in vitro cell proliferation: Part I. model development. Biotechnol. Bioeng. 109, 772–781. https://doi.org/10.1002/bit.24351.
Fauré, A., Naldi, A., Chaouiya, C., Thieffry, D., 2006. Dynamical analysis of a generic Boolean model for the control of the mammalian cell cycle. Bioinformatics 22, 124–131 https://doi.org/10.1093/bioinformatics/btl210.
Foskolou, I.P., Jorgensen, C., Leszczynska, K.B., Olcina, M.M., Tarhonskaya, H., Haisma, B., D'Angiolella, V., Myers, W.K., Domene, C., Flashman, E., Hammond, E. M., 2017. Ribonucleotide Reductase Requires Subunit Switching in Hypoxia to Maintain DNA Replication. Mol. Cell 66, 206–220. https://doi.org/10.1016/j.molcel.2017.03.005.
Gelman, A., Carlin, J., Stern, H., Dunson, D., Vehtari, A., Rubin, D., 2013. Bayesian Data Analysis. Chapman & Hall/CRC Texts in Statistical Science. CRC Press.
Good, J., Harrington, K., 2013. The hallmarks of cancer and the radiation oncologist: Updating the 5rs of radiobiology. Clin. Oncol. 25, 569–577. https://doi.org/10.1016/j.clon.2013.06.009.
Gorgoulis, V.G., Vassiliou, L.V.F., Karakaidos, P., Zacharatos, P., Kotsinas, A., Liloglou, T., Venere, M., DiTullio, R.A., Kastrinakis, N.G., Levy, B., Kletsas, D., Yoneta, A., Herlyn, M., Kittas, C., Halazonetis, T.D., 2005. Activation of the DNA damage checkpoint and genomic instability in human precancerous lesions. Nature 434, 907–913. https://doi.org/10.1038/nature03485.
Goto, T., Kaida, A., Miura, M., 2015. Visualizing cell-cycle kinetics after hypoxia/reoxygenation in HeLa cells expressing fluorescent ubiquitination-based cell cycle indicator (Fucci). Exp. Cell Res. 339, 389–396. https://doi.org/10.1016/j.yexcr.2015.10.019.
Gyllenberg, M., Webb, G.F., 1990. A nonlinear structured population model of tumor growth with quiescence. J. Math. Biol. 28, 671–694. https://doi.org/10.1007/BF00160231.
Hanahan, D., Weinberg, R.A., 2000. The hallmarks of cancer. Cell 100, 57–70. https://doi.org/10.1016/S0092-8674(00)81683-9.
Hansen, N., Müller, S.D., Koumoutsakos, P., 2003. Reducing the time complexity of the derandomized evolution strategy with covariance matrix adaptation (cma-es). Evolut. Comput. 11, 1–18. https://doi.org/10.1162/106365603321828970.
Hines, K.E., Middendorf, T.R., Aldrich, R.W., 2014. Determination of parameter identifiability in nonlinear biophysical models: A bayesian approach. J. Gen. Physiol. 143, 401–416. https://doi.org/10.1085/jgp.201311116.
Hsieh, C.H., Lee, C.H., Liang, J.A., Yu, C.Y., Shyu, W.C., 2010. Cycling hypoxia increases u87 glioma cell radioresistance via ros induced higher and long-term hif-1 signal transduction activity. Oncol. Rep. 24, 1629–1636. https://doi.org/10.3892/or_00001027.
Hsieh, C.H., Wu, C.P., Lee, H.T., Liang, J.A., Yu, C.Y., Lin, Y.J., 2012. Nadph oxidase subunit 4 mediates cycling hypoxia-promoted radiation resistance in glioblastoma multiforme. Free Radical Biol. Med. 53, 649–658. https://doi.org/10.1016/j.freeradbiomed.2012.06.009.
Johnstone, R.H., Chang, E.T., Bardenet, R., de Boer, T.P., Gavaghan, D.J., Pathmanathan, P., Clayton, R.H., Mirams, G.R., 2016. Uncertainty and variability in models of the cardiac action potential: Can we build trustworthy models? J. Mol. Cell. Cardiol. 96, 49–62. https://doi.org/10.1016/j.yjmcc.2015.11.018.
Kirkpatrick, J., Cárdenas-Navia, L., Dewhirst, M., 2004. Predicting the effect of temporal variations in po2 on tumor radiosensitivity. Int. J. Radiat. Oncol.-Biol.-Phys. 59, 822–833. https://doi.org/10.1016/j.ijrobp.2004.02.015.
Koumenis, C., Wouters, B.G., 2006. "Translating" tumor hypoxia: Unfolded protein response (UPR)-dependent and UPR-independent pathways. Mol Cancer Res. https://doi.org/10.1158/1541-7786.MCR-06-0150.
Lambert, B., 2018. A Student's Guide to Bayesian Statistics. SAGE. Publications.
Leszczynska, K.B., Dobrynin, G., Leslie, R.E., Ient, J., Boumelha, A.J., Senra, J.M., Hawkins, M.A., Maughan, T., Mukherjee, S., Hammond, E.M., 2016. Preclinical testing of an Atr inhibitor demonstrates improved response to standard therapies for esophageal cancer. Radiother. Oncol. 121, 232–238. https://doi.org/10.1016/j.radonc.2016.10.023.
Maad Sasane, S., 2016. An age structured cell cycle model with crowding. J. Math. Anal. Appl. 444, 768–803. https://doi.org/10.1016/j.jmaa.2016.06.065.
Michiels, C., Tellier, C., Feron, O., 2016. Cycling hypoxia: A key feature of the tumor microenvironment. Biochimica et Biophysica Acta (BBA) – Reviews on Cancer 1866, 76–86. doi: 10.1016/j.bbcan.2016.06.004.
Negrini, S., Gorgoulis, V.G., Halazonetis, T.D., 2010. Genomic instability an evolving hallmark of cancer. Nat. Rev. Mol. Cell Biol. 11, 220–228. https://doi.org/10.1038/nrm2858.
Olcina, M., Lecane, P.S., Hammond, E.M., 2010. Targeting hypoxic cells through the DNA damage response. Clin. Cancer Res. 16, 5624–5629. https://doi.org/10.1158/1078-0432.CCR-10-0286.
Olcina, M.M., Foskolou, I.P., Anbalagan, S., Senra, J.M., Pires, I.M., Jiang, Y., Ryan, A.J., Hammond, E.M., 2013. Replication stress and chromatin context link ATM activation to a role in DNA replication. Mol. Cell 52, 758–766. https://doi.org/10.1016/j.molcel.2013.10.019.
Pawlik, T.M., Keyomarsi, K., 2004. Role of cell cycle in mediating sensitivity to radiotherapy. Int. J. Radiat. Oncol. Biol. Phys. 59, 928–942. https://doi.org/10.1016/j.ijrobp.2004.03.005.
Pires, I.M., Bencokova, Z., Milani, M., Folkes, L.K., Li, J.A., Stratford, M.R., Harris, A.L., Hammond, E.M., 2010. Effects of acute versus chronic hypoxia on DNA damage responses and genomic instability. Cancer Res. 70, 925–935. https://doi.org/10.1158/0008-5472.CAN-09-2715.
Place, T.L., Domann, F.E., Case, A.J., 2017. Limitations of oxygen delivery to cells in culture: An underappreciated problem in basic and translational research. Free Radical Biol. Med. 113, 311–322. https://doi.org/10.1016/J.FREERADBIOMED.2017.10.003.
Ron, A., Deán-Ben, X.L., Gottschalk, S., Razansky, D., 2019. Volumetric optoacoustic imaging unveils high-resolution patterns of acute and cyclic hypoxia in a murine model of breast cancer. Cancer Res. 79, 4767–4775. https://doi.org/10.1158/0008-5472.CAN-18-3769.
Saxena, K., Jolly, M.K., 2019. Acute vs. Chronic vs. cyclic hypoxia: Their differential dynamics, molecular mechanisms, and effects on tumor progression. Biomolecules 9. https://doi.org/10.3390/biom9080339.
Sherer, E., Tocce, E., Hannemann, R., Rundell, A., Ramkrishna, D., 2008. Identification of age-structured models: Cell cycle phase transitions. Biotechnol. Bioeng. 99, 960–974. https://doi.org/10.1002/bit.21633.
Simms, K., Bean, N., Koerber, A., 2012. A Mathematical Model of Cell Cycle Progression Applied to the MCF-7 Breast Cancer Cell Line. Bull. Math. Biol. 74, 736–767. https://doi.org/10.1007/s11538-011-9700-2.
Singhania, R., Sramkoski, R.M., Jacobberger, J.W., Tyson, J.J., 2011. A Hybrid Model of Mammalian Cell Cycle Regulation. PLoS Comput. Biol. 7. https://doi.org/10.1371/journal.pcbi.1001077.
Spinelli, L., Torricelli, A., Ubezio, P., Basse, B., 2006. Modelling the balance between quiescence and cell death in normal and tumour cell populations. Math. Biosci. 202, 349–370. https://doi.org/10.1016/j.mbs.2006.03.016.
Taylor, W.R., Stark, G.R., 2001. Regulation of the G2/M transition by p53. Oncogene 2001 20:15 20, 1803–1815. https://doi.org/10.1038/sj.onc.1204252
Ubezio, P., 2004. Unraveling the complexity of cell cycle effects of anticancer drugs in cell populations. Discrete and Continuous Dynamical Systems – Series B 4, 323–335. https://doi.org/10.3934/dcdsb.2004.4.323.
Ubezio, P., Lupi, M., Branduardi, D., Cappella, P., Cavallini, E., Colombo, V., Matera, G., Natoli, C., Tomasoni, D., D'Incalci, M., 2009. Quantitative assessment of the complex dynamics of G1, S, and G2-M checkpoint activities. Cancer Res. 69, 5234–5240. https://doi.org/10.1158/0008-5472.CAN-08-3911.
Vittadello, S.T., McCue, S.W., Gunasingh, G., Haass, N.K., Simpson, M.J., 2018. Mathematical Models for Cell Migration with Real-Time Cell Cycle Dynamics. Biophys. J. 114, 1241–1253. https://doi.org/10.1016/j.bpj.2017.12.041.
Vittadello, S.T., McCue, S.W., Gunasingh, G., Haass, N.K., Simpson, M.J., 2019. Mathematical models incorporating a multi-stage cell cycle replicate normally-hidden inherent synchronization in cell proliferation. J. R. Soc. Interface 16, 20190382. https://doi.org/10.1098/rsif.2019.0382.
Vittadello, S.T., McCue, S.W., Gunasingh, G., Haass, N.K., Simpson, M.J., 2021. A novel mathematical model of heterogeneous cell proliferation. J. Math. Biol. 82, 34. https://doi.org/10.1007/s00285-021-01580-8, arXiv:2003.03024.
Weber, T.S., Jaehnert, I., Schichor, C., Or-Guil, M., Carneiro, J., 2014. Quantifying the Length and Variance of the Eukaryotic Cell Cycle Phases by a Stochastic Model and Dual Nucleoside Pulse Labelling. PLoS Comput. Biol. 10. https://doi.org/10.1371/journal.pcbi.1003616.
West, C.M., Slevin, F., 2019. Tumour Hypoxia. Clin. Oncol. 31, 595–599. https://doi.org/10.1016/j.clon.2019.06.008.
Witzel, F., Fritsche-Guenther, R., Lehmann, N., Sieber, A., Blüthgen, N., 2015. Analysis of impedance-based cellular growth assays. Bioinformatics 31, 2705–2712. https://doi.org/10.1093/bioinformatics/btv216.